Monthly Notices of the ROYAL ASTRONOMICAL SOCIETY

MNRAS **507,** 5625–5640 (2021) https://doi.org/10.1093/mnras/stab2534
Advance Access publication 2021 September 8

Comptonization by reconnection plasmoids in black hole coronae I: Magnetically dominated pair plasma

Navin Sridhar ,[1]★ Lorenzo Sironi[1] and Andrei M. Beloborodov[2,3]

[1]*Department of Astronomy and Columbia Astrophysics Laboratory, Columbia University, 550 W 120th St, New York, NY 10027, USA*
[2]*Department of Physics and Columbia Astrophysics Laboratory, Columbia University, 550 W 120th St, New York, NY 10027, USA*
[3]*Max Planck Institute for Astrophysics, Karl-Schwarzschild-Str. 1, D-85741 Garching, Germany*

Accepted 2021 September 3. Received 2021 September 3; in original form 2021 July 1

ABSTRACT

We perform 2D particle-in-cell simulations of reconnection in magnetically dominated electron–positron plasmas subject to strong Compton cooling. We vary the magnetization $\sigma \gg 1$, defined as the ratio of magnetic tension to plasma inertia, and the strength of cooling losses. Magnetic reconnection under such conditions can operate in magnetically dominated coronae around accreting black holes, which produce hard X-rays through Comptonization of seed soft photons. We find that the particle energy spectrum is dominated by a peak at mildly relativistic energies, which results from bulk motions of cooled plasmoids. The peak has a quasi-Maxwellian shape with an effective temperature of $\sim$100 keV, which depends only weakly on the flow magnetization and the strength of radiative cooling. The mean bulk energy of the reconnected plasma is roughly independent of σ, whereas the variance is larger for higher magnetizations. The spectra also display a high-energy tail, which receives $\sim$25 per cent of the dissipated reconnection power for $\sigma = 10$ and $\sim$40 per cent for $\sigma = 40$. We complement our particle-in-cell studies with a Monte Carlo simulation of the transfer of seed soft photons through the reconnection layer, and find the escaping X-ray spectrum. The simulation demonstrates that Comptonization is dominated by the bulk motions in the chain of Compton-cooled plasmoids and, for $\sigma \sim 10$, yields a spectrum consistent with the typical hard state of accreting black holes.

Key words: acceleration of particles – black hole physics – magnetic reconnection – radiation mechanisms: non-thermal – radiative transfer – relativistic processes – X-rays: binaries.

1 INTRODUCTION

The emission mechanism of high-energy non-thermal X-rays from black hole X-ray binaries (BHXBs) is still unknown. Non-thermal X-rays are predominantly seen during the so-called 'hard state' – typically observed during the onset as well as the late-time fading of an outburst. During outbursts, the X-ray luminosity increases by a few orders of magnitude, with changes in the radiation spectrum (McClintock & Remillard 2006), light-curve variability (van der Klis 1989), and possible launching of transient radio jets and collimated outflows (Mirabel & Rodríguez 1999; Fender, Belloni & Gallo 2004; Fender, Homan & Belloni 2009). An example of the transitions across different states of an outburst, and their physical origins, in the archetypal BHXB GX 339–4, is demonstrated in Sridhar et al. (2020).

A typical photon spectrum during the hard state may be roughly described as $\mathrm{d}N/\mathrm{d}E \propto E^{-\Gamma}$ with index $\Gamma \lesssim 1.8$ (where E is the photon energy) and an exponential cutoff above $\sim$100 keV. The hard X-ray emission is commonly attributed – based on the quality of spectral fits – to unsaturated Comptonization of soft photons by a cloud of hot electrons called 'corona,' with typical temperature of $\sim$100 keV (Zdziarski & Gierliński 2004).

Yet, the energization mechanism that sustains the coronal electrons against fast inverse-Compton (IC) losses is still unclear. A number of works invoked magnetic reconnection as a mechanism for heating and acceleration of electrons in black hole coronae (e.g. Galeev, Rosner & Vaiana 1979; Beloborodov 1999; Liu, Mineshige & Shibata 2002). Numerical simulations demonstrate that current sheets can form as magnetic loops get twisted by the differential rotation of the accretion flow and the black hole (Parfrey, Giannios & Beloborodov 2015; Yuan et al. 2019; Ripperda, Bacchini & Philippov 2020; Chashkina, Bromberg & Levinson 2021; Krawczynski 2021). Fig. 1 illustrates one such possible configuration. Fast magnetic reconnection ('relativistic regime') can occur in the current sheets above the accretion disc, where the energy density in magnetic fields $B^2/8\pi$ exceeds the plasma rest-mass energy density ρc^2, which corresponds to magnetization parameter $\sigma \equiv B^2/4\pi\rho c^2 > 1$ (for reviews of relativistic reconnection, see e.g. Hoshino & Lyubarsky 2012; Kagan et al. 2015). Kinetic particle-in-cell (PIC) simulations show how relativistic reconnection heats and accelerates plasma particles. Most PIC simulations have been conducted in the regime of negligible radiative losses (e.g. Zenitani & Hoshino 2001; Lyubarsky & Liverts 2008; Kagan, Milosavljević & Spitkovsky 2013; Guo et al. 2014, 2019; Sironi & Spitkovsky 2014; Nalewajko et al. 2015; Sironi, Petropoulou & Giannios 2015; Sironi, Giannios & Petropoulou 2016; Werner et al. 2016; Werner & Uzdensky 2017; Petropoulou & Sironi 2018; Hakobyan et al. 2021; Zhang, Sironi & Giannios 2021).

★ E-mail: navin.sridhar@columbia.edu

© 2021 The Author(s)
Published by Oxford University Press on behalf of Royal Astronomical Society

Downloaded from https://academic.oup.com/mnras/article/507/4/5625/6366935 by Columbia University user on 11 August 2022

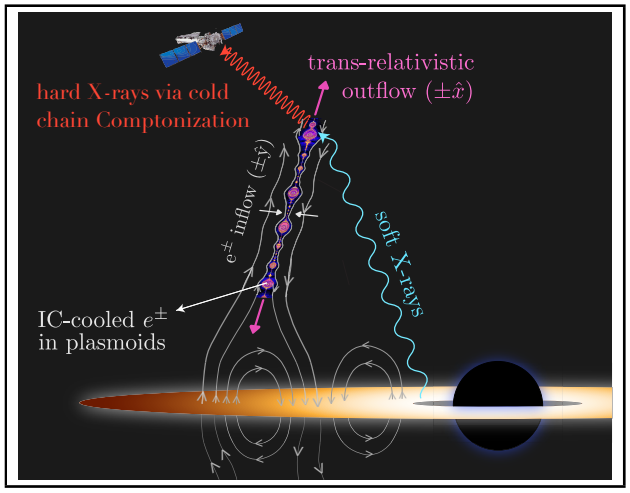

Figure 1. A schematic of the 'chain Comptonization' model. The black sphere embedded in a golden-brown disc represents the black hole-accretion disc system. Differential rotation of the magnetic field footpoints in the accretion disc leads to stretching and opening of the field lines. Two oppositely oriented fields are separated by a current sheet, and the energy in the magnetic loop is released via reconnection. This process heats the coronal particles, while the soft disc photons (blue) cool them to non-relativistic temperatures via inverse Compton (IC) scattering. Reconnection also generates a chain of coherent magnetic structures called 'plasmoids' (magenta blobs), which get accelerated to trans-relativistic speeds along the layer by magnetic tension. Comptonization of soft disc photons by the bulk motions of a cold-chain of plasmoids can reproduce the non-thermal/hard X-ray emission (red) observed from X-ray binaries.

Some recent studies have incorporated IC cooling effects, e.g. Nalewajko, Yuan & Chruślińska (2018), Werner, Philippov & Uzdensky (2019), Sironi & Beloborodov (2020) (SB20, hereafter), and Mehlhaff et al. (2020). In all these simulations, magnetic reconnection is developed through fragmentation of the dissipation layer into a chain of numerous plasmoids (magnetic islands), which move at relativistic speeds along the layer, as predicted by analytical models (Uzdensky, Loureiro & Schekochihin 2010).

Radiative cooling of electrons in luminous sources (e.g. Cygnus X-1), is very fast – the cooling time-scale is much shorter than the light-crossing time of the corona. Beloborodov (2017) pointed out that in this regime most of the plasma in the reconnection layer is kept at the local Compton temperature $kT_C \ll 100$ keV, and Comptonization of hard X-rays mainly results from the fast bulk motions of the cold plasmoid chain accelerated along the layer by the tension of magnetic field lines. Radiation exerts resistance to the plasmoid motion, as if they moved through a viscous background, and magnetic energy is passed through the plasmoids directly to photons, with subdominant heating of individual particles. Monte Carlo simulations of this Comptonization mechanism suggested an intriguing feature: it naturally gives an X-ray spectrum peaking at ~ 100 keV, consistent with the observed hard-state spectra of accreting black holes in BHXBs and Active Galactic Nuclei (AGNs).

This mechanism was further demonstrated by the kinetic plasma simulations of SB20. They found that 70–80 per cent of the reconnection power converts to radiation via Comptonization by the plasmoid bulk motions, and that these motions mimic a quasi-thermal distribution with $kT_e \sim 100$ keV. Their simulations have been performed for $e^{\pm}$ plasma with magnetization $\sigma = 10$. The dependence on σ and the possible role of ions remained unexplored.

In this paper, we extend the PIC simulations of SB20 – with strong radiative (IC) cooling – to a higher $\sigma = 40$ and quantify the dependence of particle heating and acceleration, as well as of reconnection-induced bulk motions, on the flow magnetization and the strength of cooling. In addition, we evaluate the produced X-ray spectrum with Monte Carlo simulations for $\sigma = 10$ and 40.

Like SB20, our PIC simulations are performed for $e^{\pm}$ plasma. We assume that the $e^{\pm}$ are created by the MeV photons in the tail of the Comptonized radiation spectrum, which requires a sufficiently high compactness parameter of the magnetic flare (Beloborodov 2017).

Ion density in the high-σ coronae of black holes is unknown. Since ions are not subject to radiative losses, they could store part of the released magnetic energy and gradually transfer it to the electrons. This could influence the emission mechanism of the magnetic flare. As a first step toward understanding the possible effect of ions, we perform an experiment where positrons play the role of 'ions' with mass $m_i = m_e$, and only electrons are subject to radiative losses. More realistic simulations with $m_i \gg m_e$ are more expensive and deferred to part II of this series.

The paper is organized as follows. In Section 2, we describe the numerical setup of our simulations. In Section 3, we describe the implementation and parametrization of IC cooling, and the different time-scales associated with the problem. In Section 4, we present our PIC results, emphasizing the dependence on magnetization and strength of IC cooling. The photon spectra derived from our PIC simulations using Monte Carlo radiative transfer calculations are presented in Section 5. We summarize our findings in Section 6.

2 PIC SIMULATION SETUP

The simulations are performed with the 3D electromagnetic PIC code TRISTAN-MP (Buneman 1993; Spitkovsky 2005), with particle momentum updated via the Vay pusher (Vay 2008). We employ a 2D spatial domain in the x-y plane, but all three components of velocities and electromagnetic fields are evolved. The simulation setup parallels what we have employed in, e.g. Sironi et al. (2016) and SB20. We refer to Table A1 in Appendix A for the complete set of our numerical and physical input parameters.

We consider a plasma consisting of two particle species of equal mass and opposite charge (electrons and positrons). The particles are initialized with a uniform density n_0 and a small thermal spread $kT_0/m_ec^2 = 10^{-4}$. The reconnection layer is set up with the so-called Harris equilibrium (Harris 1962), where the initial magnetic field is $B_x = -B_0 \tanh(2\pi y/\Delta)$, i.e. the field reverses at $y = 0$ across a thickness Δ. We also add a uniform magnetic field aligned with the electric current (i.e. a guide field $B_g = 0.1\,B_0$ along z). This helps providing pressure support to the cores of plasmoids, which get significantly compressed due to cooling. Note that the addition of the guide field does not add free energy to the system, as it does not get dissipated.

The field strength is parametrized by the plasma magnetization, σ. For a cold plasma – as it is in our case – we define the magnetization as

$$\sigma = \frac{B_0^2}{4\pi n_0 m_e c^2} = \left(\frac{\omega_c}{\omega_p}\right)^2, \tag{1}$$

where $\omega_c = eB_0/m_ec$ is the electron gyro-frequency, and the plasma frequency ω_p is defined as

$$\omega_p = \sqrt{\frac{4\pi n_0 e^2}{m_e}}. \tag{2}$$

Downloaded from https://academic.oup.com/mnras/article/507/4/5625/6366935 by Columbia University user on 11 August 2022

The corresponding plasma skin depth is c/ω_p. We are interested in the regime of relativistic reconnection $\sigma \gg 1$ – specifically, we consider $\sigma = 40$ (our fiducial case) and $\sigma = 10$ (SB20's reference case). The Alfvén speed is $v_A/c = \sqrt{\sigma/(\sigma+1)} \simeq 1$, i.e. close to the speed of light.

Initially, magnetic pressure outside the sheet is balanced by thermal pressure in the sheet, by adding a hot population with overdensity $\eta = 3$ relative to the number density n_0 of cold particles outside the sheet. The hot population has a temperature of $k_B T_h/m_e c^2 = \sigma/2\eta$. Reconnection is triggered by reducing the temperature of the hot particles near the centre of the domain $[(x, y) = (0, 0)]$ at the initial time. This results in the formation of a magnetic 'X-point' at the centre of the computational domain. The plasma in the current sheet separates into two reconnection fronts, that propagate away from the centre along $\pm\hat{x}$ at near the Alfvén speed. The initial current sheet thickness is chosen to be large enough ($\Delta \simeq 30\sqrt{\sigma}\, c/\omega_p$), so that the tearing mode does not spontaneously grow before the two reconnection fronts have reached the boundaries of the domain.

We employ outflow boundary conditions along x (e.g. Sironi et al. 2016), so the hot particles initialized in the sheet get evacuated after $\sim L_x/v_A$, where L_x is the half-length of the box along x. Along the y direction of the reconnection inflow, we employ two moving injectors – receding from $y = 0$ at the speed of light and continuously introducing fresh plasma and magnetic flux into the domain – and an expanding simulation box (see Sironi et al. 2016, for details). The combination of outflow boundaries in x and continuous injection in y ensures that, after $\sim$1 Alfvénic crossing time (see Appendix D for details), reconnection proceeds in a quasi-steady state, which is independent from the sheet initialization (i.e. from the choices of η and Δ), as shown by Sironi et al. (2016). We follow the evolution until $\sim 5L_x/c$, such that we have a sufficiently long time to assess the steady-state properties of the system.

A large dynamic range between plasma scales and the layer length is essential to obtain astrophysically relevant results. Our reference box for $\sigma = 40$ has $L_x/(c/\omega_p) = 3360$, but we also present results from a wide range of box sizes, $420 \le L_x/(c/\omega_p) \le 6720$. We resolve the plasma skin depth c/ω_p with 5 grid lengths. The Courant–Friedrichs–Lewy number (or equivalently, the numerical speed of light) is set to 0.45. We employ four particles per cell (including both species), and we improve particle noise in the electric current density with 32 passes of a '1-2-1' low-pass digital filter applied at each step (Birdsall & Langdon 1991).

3 INVERSE-COMPTON COOLING

Compton cooling is implemented in our code as a 'drag' force applied to the simulation particles (Tamburini et al. 2010). For an electron (or positron) with velocity $\mathbf{v}_e$ $(= \boldsymbol{\beta}_e c)$ and energy $\gamma_e m_e c^2$, the Compton drag force due to an isotropic distribution of photons is given by

$$\boldsymbol{F}_{IC} = -\frac{4}{3}\sigma_T \gamma_e^2 U_{rad} \boldsymbol{\beta}_e, \tag{3}$$

where $\sigma_T = 8\pi e^4/(3m_e^2 c^4)$ is the Thomson cross-section, $\gamma_e = (1 - \beta_e^2)^{-1/2}$ is the particle Lorentz factor, and U_{rad} is the radiation energy density. We parametrize U_{rad} by defining a critical Lorentz factor γ_{cr}, at which the Compton drag force balances the force due to the reconnection electric field $E_{rec} = \eta_{rec} B_0$, where $\eta_{rec} \sim 0.1$ is the reconnection rate. For $|\beta_e| \simeq 1$, the balance

$$e E_{rec} = \frac{4}{3}\sigma_T \gamma_{cr}^2 U_{rad} \tag{4}$$

yields $\gamma_{cr} \equiv \sqrt{3e\eta_{rec} B_0/(4\sigma_T U_{rad})}$. A low value of γ_{cr} implies strong cooling (i.e. large U_{rad}). In contrast, the limit of negligible cooling losses ($U_{rad} = 0$) corresponds to $\gamma_{cr} = \infty$. For our reference magnetization $\sigma = 40$, we investigate $\gamma_{cr} = 16$, 22.6, 32, 45, and the uncooled case $\gamma_{cr} = \infty$.

The IC cooling time for a particle with Lorentz factor γ_e can be written as

$$t_{IC}(\gamma_e) = \frac{3m_e c}{4\sigma_T U_{rad}\gamma_e} = \frac{1}{\omega_c}\frac{\gamma_{cr}^2}{\eta_{rec}\gamma_e}. \tag{5}$$

This should be compared with the temporal resolution of our simulations

$$\Delta t = 0.09\,\omega_p^{-1} = 0.09\,\sigma^{1/2}\omega_c^{-1}. \tag{6}$$

This shows that the IC cooling time for a particle with Lorentz factor as high as $\gamma_e = \gamma_{cr}$ is well resolved if

$$\frac{\Delta t}{t_{IC}(\gamma_{cr})} \sim 10^{-2}\frac{\sigma^{1/2}}{\gamma_{cr}} \ll 1\,. \tag{7}$$

This condition is well satisfied in our simulations, which all have $\gamma_{cr} > \sqrt{\sigma}$ (see Table A1 in Appendix A).

3.1 Energy and time-scales

Here, we summarize the hierarchy of energy and time-scales of radiative reconnection in BHXB coronae. We refer to Beloborodov (2017) and SB20 for additional details.

As long as the Thomson optical depth of the reconnection layer is not much greater than unity ($\tau_T \sim 1$ is typically inferred for black hole coronae[1]), energy conservation implies that the radiation density is $U_{rad} \sim \eta_{rec} U_B \sim 0.1\,U_B$, where $U_B = B_0^2/8\pi$ is the energy density of the reconnecting field. The magnetization parameter σ can be expressed as

$$\sigma = \frac{2U_B}{n_0 m_e c^2} \sim \frac{2\eta_{rec}\ell_B}{\tau_T}, \tag{8}$$

where $\ell_B = U_B \sigma_T L_x/m_e c^2$ is the magnetic compactness. For magnetic flares near black holes accreting at a significant fraction of the Eddington limit, the magnetic compactness can approach $\ell_B \sim m_p/m_e$ (Beloborodov 2017). Using $\eta_{rec} \sim 0.1$ and $\tau_T \sim 1$, equation (8) gives $\sigma \sim 200\,(\ell_B/10^3)$.

Given that $U_{rad} \sim \eta_{rec} U_B$, we can quantify the expected value of γ_{cr} as

$$\gamma_{cr} = \left(\frac{27\,L_x}{16\,\ell_B r_e}\right)^{1/4} \sim 10^4\left(\frac{M_{BH}}{10M_\odot}\right)^{1/4}, \tag{9}$$

where r_e is the classical electron radius, $\ell_B \sim m_p/m_e$ and we have assumed that the characteristic length of reconnection layers is $L_x \sim r_g$, where $r_g = 2GM_{BH}/c^2$ is the Schwarzschild radius for a black hole of mass M_{BH}.

Accelerated particles typically attain a Lorentz factor $\gamma_X \sim \sigma/4$ at X-points. A high value of $\gamma_{cr} \gg \gamma_X \sim \sigma/4$ then implies that particle acceleration at X-points is not impeded by Compton drag. The same condition can be expressed by comparing the IC cooling time-scale for particles with $\gamma_e = \gamma_X$ with the time-scale t_X for particle acceleration at X-points,

$$\frac{t_{IC}(\gamma_X)}{t_X} = \frac{\gamma_{cr}^2}{\gamma_X^2} \gg 1, \qquad t_X = \frac{\gamma_X m_e c}{e E_{rec}}\,. \tag{10}$$

[1]The optical depth across the layer is $\tau_T = H n_0 \sigma_T$, where $H \sim \eta_{rec} L_x$ is the thickness of the reconnection layer.

Downloaded from https://academic.oup.com/mnras/article/507/4/5625/6366935 by Columbia University user on 11 August 2022

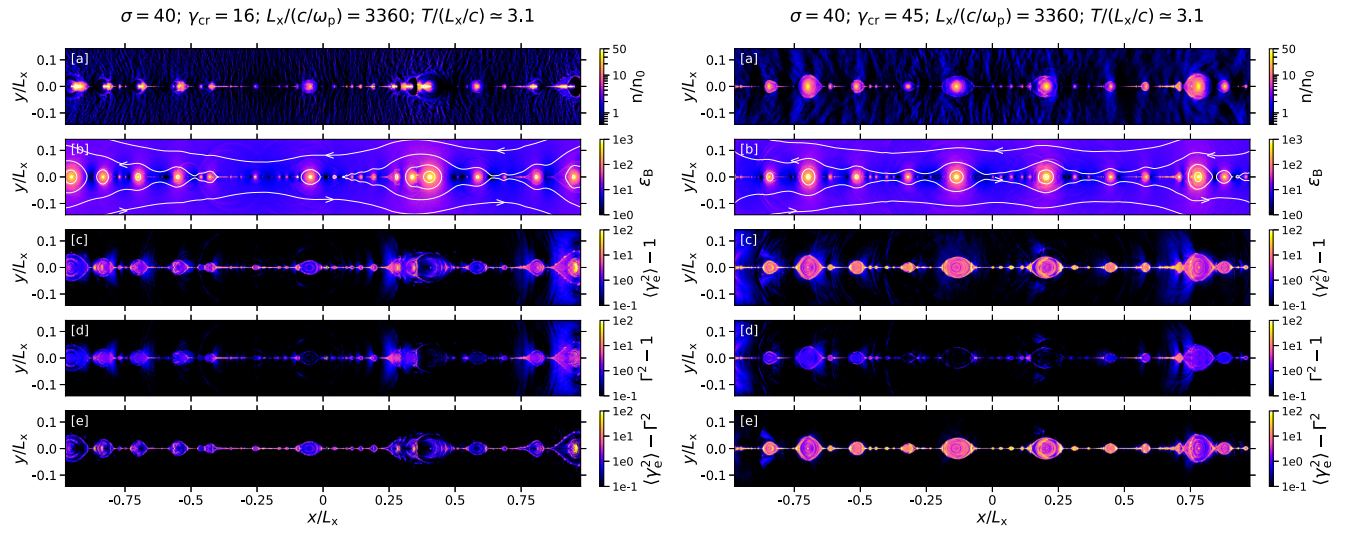

(i) Strong IC cooling (ii) Moderate IC cooling

Figure 2. Snapshot of the reconnection layer at time $T \simeq 3.1 L_x/c \simeq 10621\ \omega_p^{-1}$ for our fiducial model ($\sigma = 40$ and $L_x = 3360 c/\omega_p$) with strong cooling ($\gamma_{cr} = 16$, left-hand panel) and moderate cooling ($\gamma_{cr} = 45$, right-hand panel). We only show the region $|y| \leq 0.15\, L_x$ where reconnection occurs. (a) Particle number density n in units of the initialized (upstream) number density n_0. (b) Magnetic energy density $B^2/8\pi$ normalized to the upstream plasma rest mass density, $\varepsilon_B = B^2/8\pi n_0 m_e c^2$. The overplotted white contours are magnetic field lines. (c) Local average $\langle \gamma_e^2 \beta_e^2 \rangle = \langle \gamma_e^2 \rangle - 1$, which is proportional to the IC power per particle (the local average is calculated using the patches of 5×5 cells). (d) $\Gamma^2 - 1$, where Γ is the bulk Lorentz factor defined in the text. (e) $\langle \gamma_e^2 \rangle - \Gamma^2$, which represents internal particle motions. The quantities shown in panels (a), (c), (d), and (e) are computed using both electrons and positrons.

On the other hand, the IC cooling time is much shorter than the advection time along the layer $t_{adv} \sim L_x/v_A \sim L_x/c$. Their ratio is

$$\frac{t_{IC}(\gamma_e)}{t_{adv}} = \frac{3}{4\gamma_e \ell_{rad}} \ll 1, \tag{11}$$

where the radiation compactness is defined as $\ell_{rad} = U_{rad}\sigma_T L_x/m_e c^2 = \eta_{rec}\ell_B$. We rewrite the ratio of time-scales as

$$\frac{t_{IC}(\gamma_e)}{t_{adv}} = \frac{\tau_{cool}}{\gamma_e}. \tag{12}$$

Then, the condition that the time to cool down to non-relativistic energies is shorter than the advection time-scale may be expressed as

$$\tau_{cool} \equiv \frac{\gamma_{cr}^2}{\eta_{rec}\sqrt{\sigma}} \frac{c/\omega_p}{L_x} < 1\,. \tag{13}$$

In our simulations, we explore both $\tau_{cool} < 1$ and $\tau_{cool} > 1$ regimes. In the latter case, τ_{cool} equals the Lorentz factor of particles that cool in a dynamical (advection) time. We use τ_{cool} (as an alternative to γ_{cr}) to quantify the strength of cooling losses.

In the limit of strong cooling, particles in reconnection plasmoids are cooled down to non-relativistic temperatures ($\gamma_e \approx 1$), well before the plasmoid bulk motions are decelerated by Compton drag (Beloborodov 2017). For the cold particles, the ratio of drag time to advection time is

$$\frac{t_{drag}}{t_{adv}} \sim \frac{\sigma m_e c}{U_{rad}\sigma_T} \Big/ \frac{L_x}{c} \sim \frac{\sigma}{\ell_{rad}}. \tag{14}$$

Given that $\sigma \sim \eta_{rec}\ell_B/\tau_T \sim \ell_{rad}/\tau_T$ (equation 8), one can see that the two time-scales are comparable for $\tau_T \sim 1$. Their ratio may also be written as $t_{drag}/t_{adv} \sim \sigma\tau_{cool}$ when $\gamma_e \approx 1$.

In summary, in order to mimic the conditions in black hole coronae, our simulations have to retain the following hierarchy of energy and time-scales: (*i*) $\sigma \gg 1$; (*ii*) $\gamma_{cr} \gg \gamma_X \sim \sigma/4$, or equivalently particle acceleration at X-points occurs faster than IC cooling losses; (*iii*) $\tau_{cool} \ll 1$, or equivalently the IC cooling time for all particles is shorter than the advection time along the layer. Most of our simulations do satisfy the required hierarchy.

4 PIC SIMULATION RESULTS

In this section, we present the main results of our PIC simulations. We discuss how our PIC results depend on the strength of radiative IC losses, magnetization, and domain size. Our fiducial runs have $\sigma = 40$ and $L_x/(c/\omega_p) = 3360$.

In Section 4.1, we describe the general structure of the reconnection layer. We then explore the influence of radiative cooling on internal and bulk motions in Section 4.2. Particle energy spectra are presented in Section 4.3. In Section 4.4, we probe the structure of the reconnection layer and the particle energy spectrum in a 'hybrid' experiment, where we consider a pair plasma, but only cool electrons. This is a first step towards understanding radiative reconnection in an electron–ion plasma, where only electrons suffer IC cooling losses.

4.1 Structure of the reconnection layer

In Fig. 2, we present the 2D structure of the reconnection layer in the strongly magnetized model with $\sigma = 40$ for two different levels of IC cooling: strong cooling with $\gamma_{cr} = 16$ on the left, and moderate cooling with $\gamma_{cr} = 45$ on the right. Regardless of the cooling strength, the reconnection layer fragments into a hierarchical chain of coherent structures (plasmoids) separated by X-points, as a result of the tearing instability (Tajima & Shibata 1997; Loureiro, Schekochihin & Cowley 2007; Bhattacharjee et al. 2009; Uzdensky et al. 2010).

Plasmoid mergers lead to the formation of secondary reconnection layers transverse to the main layer. An example of such transverse layers can be seen at $x/L_x \sim 0.35$ in the left-hand panel of Fig. 2.

Downloaded from https://academic.oup.com/mnras/article/507/4/5625/6366935 by Columbia University user on 11 August 2022

Overall, the formation of the plasmoid chain proceeds independently of the degree of IC cooling. We have also verified that in our $\sigma = 40$ runs, the reconnection rate and the distribution of plasmoid sizes (see Appendix B) are not significantly affected by cooling, similar to the lower magnetization case ($\sigma = 10$) discussed by SB20.

In the case of moderate cooling (right-hand panel (a) in Fig. 2), particles are nearly symmetrically distributed in plasmoids (i.e. front and back sides are equally populated). On the other hand, under strong cooling, the plasma density distribution inside plasmoids becomes strongly non-uniform (left-hand panel (a)). A near-vacuum region develops at the plasmoid 'head' – along the direction of motion – leaving a 'tail' of piled-up particles on the back side. This effect is caused by Compton drag on the particles. Since the particles can freely slide along magnetic field lines, Compton drag pushes them towards the back of the moving plasmoid. The cavities are most pronounced inside plasmoids that are farther from the centre, because they typically move faster and have lived longer, allowing more time for the drag.

The 2D structure of magnetic energy density ($\epsilon_B = B^2/8\pi n_0 m_e c^2$; panels (b) of Fig. 2) is similar in models with different levels of cooling. In particular, the boundaries of plasmoids, defined as regions of large ϵ_B, have similar shapes, and the peak value of ϵ_B inside the plasmoids is also nearly the same. This peak occurs in the cores (O-points) of plasmoids, and their measured values for the largest plasmoids are $\epsilon_B \sim 7 \times 10^3$. Note that the normalized magnetic energy density in the inflow region is $\epsilon_B \sim \sigma/2 \sim 20$. Hence, the magnetic field in the plasmoid cores has been compressed by a factor of $B/B_0 \sim 18$ relative to the upstream field. The similarity of plasmoid chains in all cooling models confirms that the chain structure is controlled by magnetic stresses, with small effects of plasma pressure. In short, plasmoids in relativistic reconnection are fundamentally magnetic structures.

In panels (c), we plot the local average $\langle \gamma_e^2 \beta_e^2 \rangle = \langle \gamma_e^2 \rangle - 1$, which is proportional to the IC power per particle. In the strongly cooled case, the plasma has lost most of the energy received from reconnection, so $\langle \gamma_e^2 \beta_e^2 \rangle$ is strongly reduced. For both strong and moderate cooling, we find that $\langle \gamma_e^2 \beta_e^2 \rangle$ is highest in the thin regions of the reconnection layer (the sites of X-points and fast outflows emanating from them) and the heads and tails of the plasmoids. Note that significant dissipation occurs at the plasmoid boundaries, because of (*i*) mergers and (*ii*) the release of kinetic energy via the slowdown of outflows launched from a neighbouring X-point and entering the plasmoid.

In panel (d), we isolate the contribution due to bulk motions alone. For every cell, we calculate the average particle velocity $\boldsymbol{\beta} = \langle \boldsymbol{\beta}_e \rangle$ including all electrons and positrons in the local patch of 5×5 cells. In the frame moving with velocity $\boldsymbol{\beta}$, the plasma stress–energy tensor has a vanishing energy flux (e.g. Rowan, Sironi & Narayan 2019), and we define it as the comoving frame of the plasma. The corresponding bulk Lorentz factor is $\Gamma = (1 - \beta^2)^{-1/2}$. We find that the bulk motions of large plasmoids weakly depend on the cooling strength. The plasmoids move nearly as rigid bodies, and their speed on average grows with distance from the centre of the layer. This growth is somewhat limited by Compton drag in the model with strongest cooling, which results in a slightly slower outflow. Young plasmoids develop high speeds, as they are pulled toward large plasmoids. Fast bulk motions also occur in the tails of plasmoids that accrete the reconnected plasma from nearby X-points (see e.g. the plasmoid at $x/L_x \sim -0.7$ in the right-hand panel). Besides the motions along the layer, we observe high bulk speeds in the secondary reconnection layers generated by plasmoid mergers (e.g. at $x/L_x \sim 0.35$ in the left-hand panel).

In the case of strong cooling (left-hand column), the similarity between panels (c) and (d) suggests that most of the IC power comes from bulk motions. The effect of internal motions of individual particles may be quantified by the difference $\langle \gamma_e^2 \rangle - \Gamma^2$ (panel e). In the case of moderate cooling, internal motions dominate over bulk motions almost everywhere in the reconnection layer. In the model with strong cooling, internal motions are suppressed inside plasmoids down to a non-relativistic temperature. This is especially true for large plasmoids, which are long-lived, so their particles have plenty of time to radiate away their energy.[2] High-temperature internal motions are predominant in the thin regions of the main reconnection layer (and secondary layers generated by plasmoid mergers) where particles have been recently energized and are yet to cool down.[3] As shown by SB20, particles accelerated at X-points or 'picked up' by the fast reconnection outflows are energized on a time-scale shorter than the IC cooling time.

4.2 Bulk and internal motions

We now explore in more detail how the bulk and internal motions depend on the flow magnetization and the cooling level. We exclude the cold, slow inflow and examine motions in the 'reconnection region,' which is defined using the following density-mixing criterion (e.g. Rowan, Sironi & Narayan 2017; Ball, Sironi & Özel 2018): the region that contains a mixture of particles coming from above and below the reconnection midplane $y = 0$, with both populations contributing at least 1 per cent to the mixture. All results presented below refer to particles and cells from this region unless otherwise specified.

First, we calculate the bulk 4-velocities parallel ($u_x = \Gamma \beta_x$) and orthogonal ($u_y = \Gamma \beta_y$) to the reconnection layer. Fig. 3 shows the distributions of u_x and u_y measured across different cells. To ensure sufficient statistics, we only use cells containing $\geq$4 particles, and the distributions are averaged over time interval $2 \lesssim T/(L_x/c) \lesssim 5$, when reconnection proceeds in a quasi-steady state. Fig. 3 presents the resulting distributions in the $x - u_x$ space (left-hand panel) and in the $u_x - u_y$ space (right-hand panel), for a sequence of models with different cooling levels.

The observed behaviour in our fiducial model with $\sigma = 40$ is similar to the model with $\sigma = 10$ described in SB20. Bulk motions are primarily oriented along the layer, i.e. they are dominated by u_x. The mean value of $u_x(x)$ is nearly independent of the cooling level. It starts from zero near the centre of the layer and approaches a constant value $|u_x| \sim 1$ at $|x|/L_x \gtrsim 0.25$. Most of the reconnected plasma moves with transrelativistic $|u_x| \sim 1$. Only a small fraction moves with ultrarelativistic bulk speeds, approaching the Alfvénic limit (Lyubarsky 2005): $|u_x| \approx \sqrt{\sigma} \approx 6.3$ (only small plasmoids can reach $|u_x| \approx \sqrt{\sigma}$, as discussed in Appendix B). We note that this fast fraction is reduced for (i) stronger cooling, due to Compton drag, and (ii) larger magnetization $\sigma = 40$, compared with the $\sigma = 10$ model investigated by SB20; a similar effect was discussed by Sironi et al. (2016) for uncooled simulations.

A fraction of the reconnected plasma is flowing towards the centre of the layer (i.e. opposite to the mean motion). This is seen in Fig. 3 [left-hand panel] as localized spikes with $u_x < 0$ at $x > 0$ (and $u_x >$

[2]The effect of IC cooling on plasmoids as a function of their size in investigated in Appendix B.

[3]Significant internal motions are also observed near the core of merging plasmoids, likely due to compression (e.g. see the bright regions in panel (e) of the left-hand column at $x/L_x \sim 0.3$ and 0.9).

Downloaded from https://academic.oup.com/mnras/article/507/4/5625/6366935 by Columbia University user on 11 August 2022

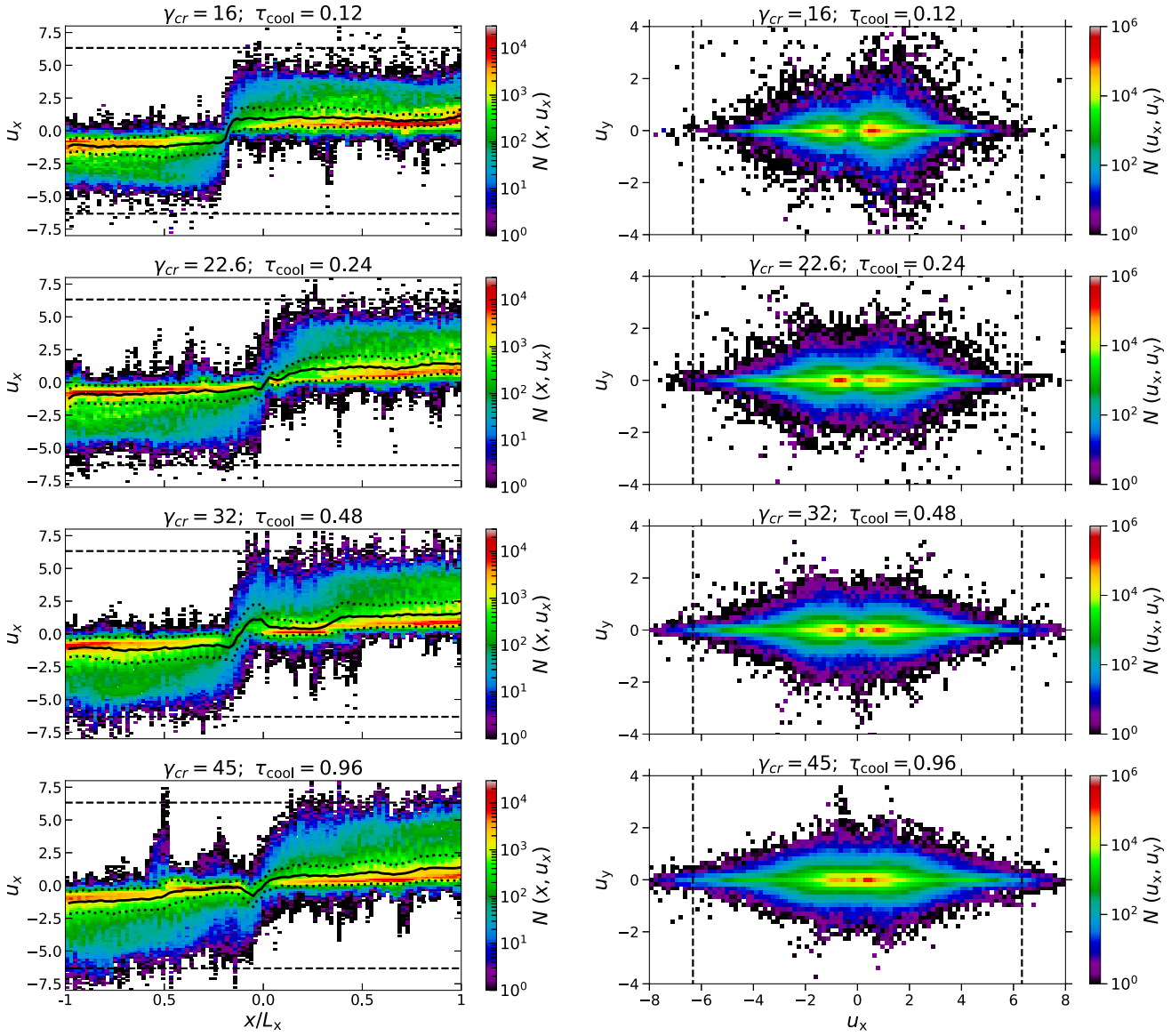

Figure 3. Left-hand panel: bulk motions along the reconnection layer, viewed in the phase space $x - u_x$. Colour represents particle density in the phase space. The measurements were made for our fiducial model with $\sigma = 40$, $L_x/(c/\omega_p) = 3360$, and different panels correspond to different levels of cooling: $\gamma_{cr} = 16$, 22.6, 32, 45 (strongest to weakest from top to bottom). The solid black curve in each panel shows the mean value of u_x as a function of x, and the black dotted curves show the standard deviation around the mean. Right-hand panel: bulk motions along x and y, viewed in the momentum space $u_x - u_y$, for the same simulations as in the left-hand panels. Colour represents the particle density in the $u_x - u_y$ space. In all (left-hand and right-hand) panels, the black dashed lines indicate the Alfènic limit $\sqrt{\sigma}$. The distributions were time-averaged during the time interval $2 \lesssim T/(L_x/c) \lesssim 5$, when the reconnection layer was in a quasi-steady state.

0 at $x < 0$). These motions are caused by large plasmoids attracting and accreting small young plasmoids ahead of them. As a result, a small fraction of plasma motions opposite to the mean outflow motion.

The stochastic character of plasmoid motions plays an important role for Comptonization calculations (see Section 5) and it is further quantified in Fig. 4. We use half of the reconnection region ($x > 0$), and compute the global mean and standard deviation of the bulk 4-velocity u_x for $\sigma = 10$ and 40 and for a variety of cooling levels, $0.06 \lesssim \tau_{cool} \lesssim 1.0$. For each σ and τ_{cool}, we show the result for the largest available simulation (which also has the highest γ_{cr}, see equation 13). We verified that the results remain nearly the same when varying L_x and γ_{cr} for given σ and τ_{cool} (see Appendix A).

One can see from Fig. 4 that the global mean $\langle u_x \rangle \sim 1$ is similar in all models, and the standard deviation has a significant systematic dependence on both τ_{cool} and σ: it increases for larger τ_{cool} (i.e. weaker cooling) and for higher σ. Thus, bulk motions are more ordered for lower magnetizations and stronger cooling. The dispersion in bulk motions for $\sigma = 40$ is roughly twice that for $\sigma = 10$, at a given τ_{cool}.

Bulk motions in the y-direction (orthogonal to the main reconnection layer) are quantified by the distribution in the $u_x - u_y$ space (Fig. 3 [right-hand panel]). The u_y component is mostly produced by the secondary transverse reconnection layers created during plasmoid mergers. Most mergers occur between plasmoids with moderate x-velocities, which explains why the largest u_y are observed at moderate

Downloaded from https://academic.oup.com/mnras/article/507/4/5625/6366935 by Columbia University user on 11 August 2022

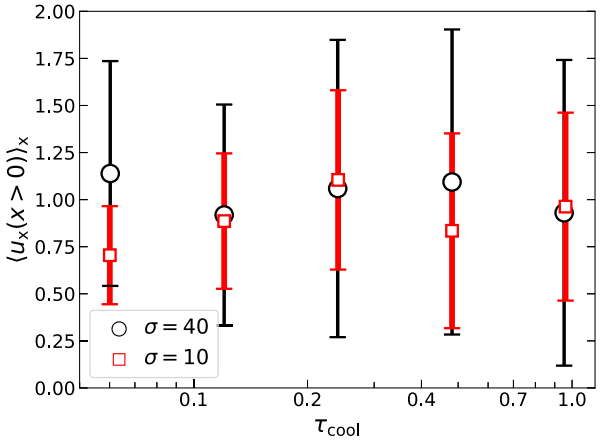

Figure 4. Statistics of bulk motions along the reconnection layer in the models with various τ_{cool}, for $\sigma = 10$ (red) and $\sigma = 40$ (black). The red squares and black circles indicate the mean (density-weighted) bulk 4-velocity u_x for $\sigma = 10$ and 40 respectively, and the error bars indicate its standard deviation. The measurements were performed along one half of the reconnection layer ($x > 0$) and averaged during the time interval $2 \lesssim T/(L_x/c) \lesssim 5$.

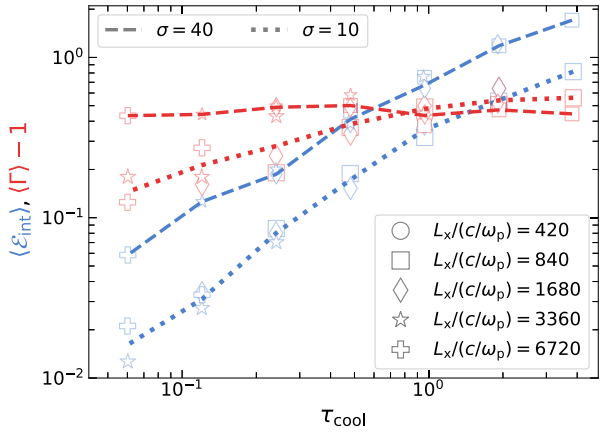

Figure 5. Average particle energy (in units of $m_e c^2 = 511$ keV) resolved into two components: internal (blue) and bulk (red), plotted versus τ_{cool}. The dashed curves refer to $\sigma = 40$, and dotted to $\sigma = 10$. For given σ and τ_{cool}, different symbols correspond to different sizes of the simulation domain (see legend), which equivalently correspond to different γ_{cr}. Where more than one simulation is available with the same σ and τ_{cool} (Table A1), the curve passes through the mean value. The measurements were performed using density-weighted averaging over the reconnection region and averaging over time interval $2 \lesssim T/(L_x/c) \lesssim 5$.

u_x. However, overall the y-motions in the reconnection layer are weaker than the x-motions, and u_y never reaches the Alfvén limit. This may be explained by the fact that the transverse reconnection layers are shorter than the main layer (their extent is limited by the width of the largest plasmoids, $\sim 0.1\,L_x$), and the reconnected plasma may fail to reach the expected Alfvén limit. In addition, the secondary reconnection occurs in already heated plasma, which tends to reduce the effective magnetization and the corresponding Alfvén speed in the layers between merging plasmoids. However, strong cooling increases the local magnetization, and so models with lower τ_{cool} display faster y-motions. Furthermore, strong Compton drag creates density cavities (see Section 4.1), boosting the local magnetization parameter. Overall, the reduced temperature and density result in faster reconnection outflows.

Next, we examine how the energy in bulk motions compares with the internal energy of the plasma (heat). In each cell, the mean bulk energy per particle (in units of the rest mass energy) is simply $\Gamma - 1$. The mean internal energy per particle is obtained as described in Appendix C (e.g. Rowan et al. 2017). We Lorentz boost the particle energy density from the simulation frame to the plasma rest frame, which moves at velocity $\boldsymbol{\beta}$. The mean internal energy per particle $\mathcal{E}_{int}$ (normalized to the rest mass energy) is then calculated assuming that the pressure tensor is isotropic in the plasma rest frame. Using the values obtained in each cell, we find the global mean values $\langle\Gamma - 1\rangle$ and $\langle\mathcal{E}_{int}\rangle$, first by (density-weighted) averaging over the reconnection region, and then by time-averaging over the interval $2 \lesssim T/(L_x/c) \lesssim 5$.

Fig. 5 shows how the measured $\langle\Gamma - 1\rangle$ and $\langle\mathcal{E}_{int}\rangle$ depend on τ_{cool}.[4] The similarity of bulk motions in all models of $\sigma \gg 1$ and IC cooling results in a nearly universal $\langle\Gamma - 1\rangle \sim 0.4$. The only exception is the decrease observed in the strongest cooling cases of $\sigma = 10$, down to $\langle\Gamma - 1\rangle \sim 0.1$ for $\tau_{cool} = 0.06$. This decrease is the result of Compton drag. Since the ratio of drag time to advection time is $t_{drag}/t_{adv} \sim \sigma\,\tau_{cool}$ (see equations 14 and Section 3.1), we expect Compton drag to affect the average bulk motions when $\tau_{cool} \lesssim \sigma^{-1}$.

As one can see from Fig. 5, the 'hot regime' with $\langle\mathcal{E}_{int}\rangle > \langle\Gamma - 1\rangle$ occurs for large τ_{cool}, namely $\tau_{cool} \gtrsim 1$ for $\sigma = 10$ and $\tau_{cool} \gtrsim 0.5$ for $\sigma = 40$. In the limit of negligible cooling losses, the mean internal energy per particle $\langle\mathcal{E}_{int}\rangle$ should approach the mean Lorentz factor $\sim\sigma/4$ of particles heated by reconnection. We speculate that this asymptotic limit should be approached when $\tau_{cool} \gtrsim \sigma/4$, i.e. when the majority of particles heated/accelerated by reconnection do not appreciably cool before advecting out of the system.[5]

4.3 Particle energy spectra

In this section, we investigate how the particle energy spectrum varies with σ and cooling strength. Note that the cooling effects depend on the cooling rate (parametrized by γ_{cr}) and the characteristic time L_x/c available for cooling before the particles are advected out of the layer. Therefore, we examine the dependence on both γ_{cr} and L_x.

For each particle, we identify the energy contribution from the local bulk motion. Then, we can compare the spectrum of bulk motions with the total energy spectrum and see where bulk motions dominate. The spectra are extracted from the reconnection region and averaged in time over the interval $2 \lesssim T/(L_x/c) \lesssim 5$, when the layer has achieved a quasi-steady state. They are normalized by L_x^2 to allow a fair comparison of simulations with different L_x.

Fig. 6 presents the results for $\sigma = 40$. Each row corresponds to a chosen value of γ_{cr} (increasing from top to bottom; so, the cooling rate decreases from top to bottom), and each column has a chosen domain size (increasing from left to right). The parameter $\tau_{cool} \propto \gamma_{cr}^2/L_x$ varies diagonally (bottom left-hand to upper right-hand) in this 4×3 set of models. For completeness, we present in Fig. 7 the corresponding simulations without cooling, i.e. $\gamma_{cr} = \infty$.

[4]Fig. 5 also demonstrates that variations in γ_{cr} and L_x do not appreciably change the results as long as they give the same τ_{cool}. This fact is not surprising, as variation in $\gamma_{cr} \gg \sigma/4$ directly affects only very energetic particles, with Lorentz factors far beyond the mean post-reconnection value $\sim\sigma/4$.

[5]We remind that for $\tau_{cool} > 1$, the cooling parameter τ_{cool} equals the Lorentz factor of particles that cool in a dynamical (advection) time.

Downloaded from https://academic.oup.com/mnras/article/507/4/5625/6366935 by Columbia University user on 11 August 2022

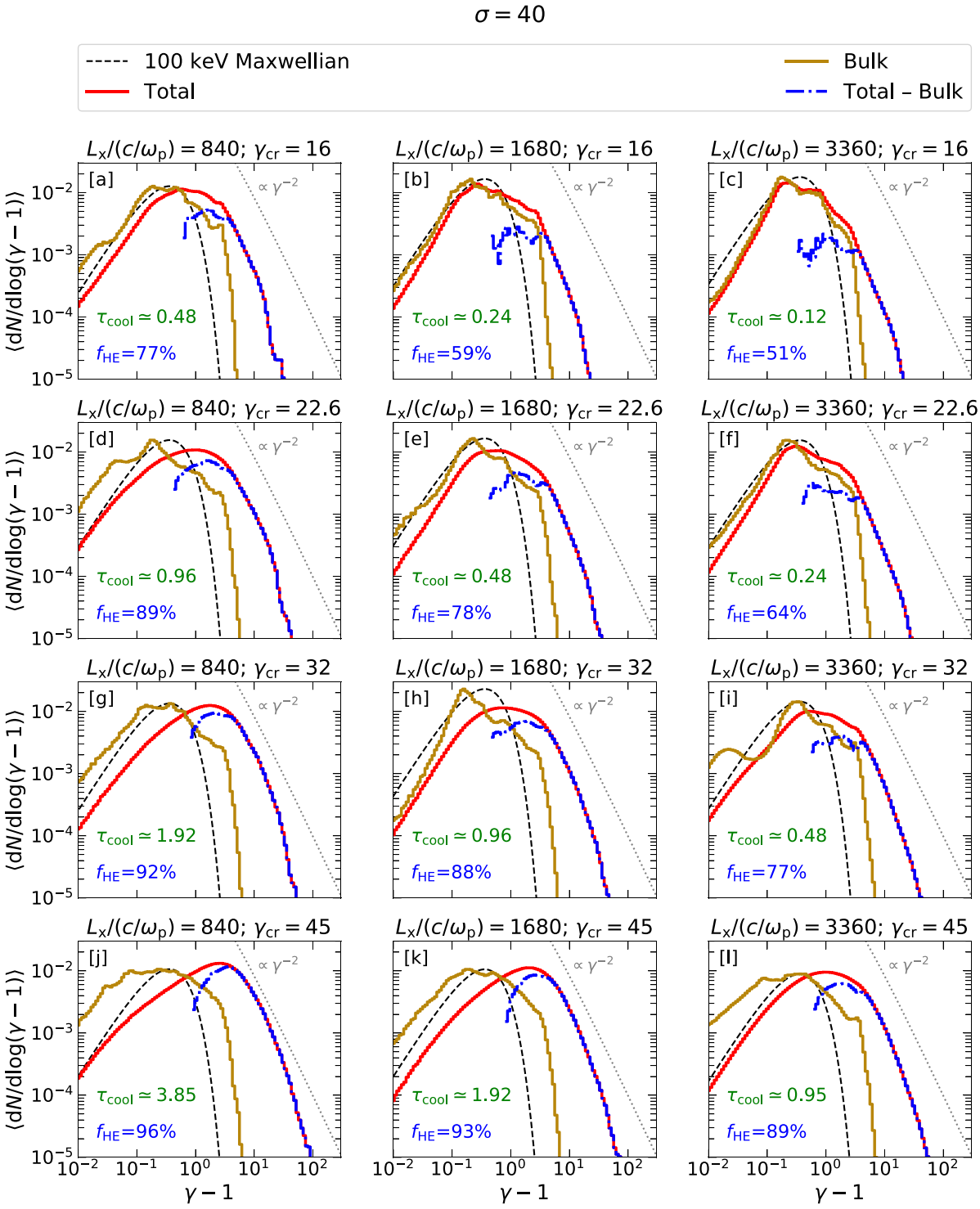

Figure 6. Particle energy spectra extracted from the reconnection region and averaged over time $2 \lesssim T/(L_x/c) \lesssim 5$. Twelve simulations are shown with magnetization $\sigma = 40$ and different values of γ_{cr} and domain size L_x. The background radiation density decreases from top to bottom (γ_{cr} increases from 16 to 45) while the domain size increases from left to right (from $L_x = 840\,c/\omega_p$ to $L_x = 3360\,c/\omega_p$). The corresponding value of τ_{cool} is indicated in each panel. The spectra are normalized by L_x^2 for proper comparison of models with different L_x. Each panel shows the total energy spectrum (red; $\gamma = \gamma_e$), the bulk motion spectrum (golden-brown; $\gamma = \Gamma$), and their difference (dash-dotted blue), i.e. the part not accounted for by bulk motions; the fractional IC power contributed by this component is denoted in each panel as f_{HE}. For comparison, we also plot a Maxwellian distribution with temperature of 100 keV (dashed black), normalized so that its peak matches the peak of the bulk energy spectrum. The dotted grey lines indicate the -2 slope that corresponds to equal IC power per decade in Lorentz factor.

Downloaded from https://academic.oup.com/mnras/article/507/4/5625/6366935 by Columbia University user on 11 August 2022

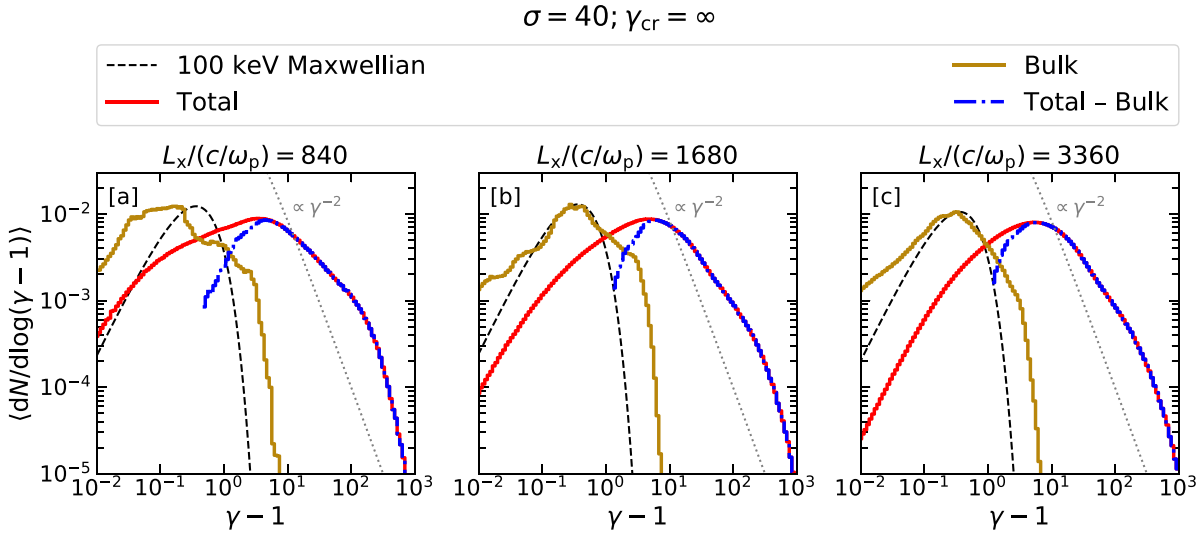

Figure 7. Same as in each row of Fig. 6, but for the simulations without cooling ($\gamma_{cr} = \infty$).

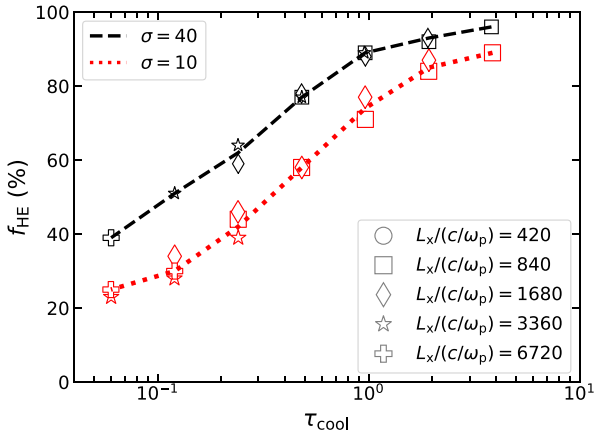

Figure 8. Fraction of the IC power contributed by high-energy particles f_{HE} versus τ_{cool}, measured in the simulations with $\sigma = 10$ (red dotted) and $\sigma = 40$ (black dashed). Each data point was calculated by averaging over the reconnection region and then averaging over the time interval $2 \lesssim T/(L_x/c) \lesssim 5$. Different symbols represent simulations with different domain sizes L_x (see legend) or, equivalently, different γ_{cr}. The curves show the average result of all simulations available for given σ and τ_{cool}.

In the absence of IC cooling (Fig. 7), the total particle spectrum peaks at $\gamma_e - 1 \sim 10 \sim \sigma/4$ regardless of the domain size, and the mean Lorentz factor of particles heated by reconnection is determined by energy conservation, $\bar{\gamma}_e \approx \sigma/4$. With increasing cooling, the spectral peak progressively shifts to lower values (Fig. 6). Its position and shape are primarily controlled by τ_{cool}. In fact, the total particle spectra for simulations with the same τ_{cool} are remarkably similar. At $\tau_{cool} \ll 1$, the strong cooling results in a non-relativistic temperature (see also Fig. 5), and the total energy spectrum converges towards the bulk energy spectrum, i.e. the particle energies are dominated by the bulk motions. This is especially clear in the top right-hand panel, which has the lowest $\tau_{cool} \simeq 0.12$.

While the total energy spectrum changes drastically for different levels of cooling, the bulk energy spectrum is barely affected. In the absence of IC cooling ($\gamma_{cr} = \infty$), the peak of the distribution of bulk motions is typically at $\Gamma - 1 \sim 0.3$ (Figs 7b, c).[6] Remarkably, the peak of the bulk spectrum is approximately the same ($\Gamma - 1 \sim 0.3$) regardless of the cooling strength. This behaviour of bulk motions is in agreement with Fig. 5. For all our simulations, the shape of the bulk spectrum resembles a Maxwell–Jüttner distribution, and its effective temperature is not far from $kT_e \sim 100$ keV. Thus, the spectrum of bulk motions of a Compton-cooled plasmoid chain mimics a thermal plasma with a mildly relativistic temperature.

At high energies, the total particle spectrum cannot be accounted for by bulk motions alone; instead, it becomes dominated by internal motions (Figs 6 and 7). The high-energy particles are observed in the thin regions of the main reconnection layer and the secondary layers generated by plasmoid mergers (see Fig. 2e, left-hand panel). They are present even in the case of strongest cooling ($\tau_{cool} \ll 1$), and such particles need to be sustained by a process of non-thermal particle acceleration operating on time-scales shorter than the cooling time. Their origin is described by SB20: the particles are energized either by the non-ideal reconnection electric field at X-points or by being picked up by fast reconnection outflows from the X-points.

We define the high-energy component of the particle spectrum as the difference between the total and bulk spectra, as shown in Figs 6 and 7. This component radiates an interesting fraction f_{HE} of the total IC luminosity from the reconnection layer. The value of f_{HE} is quoted in each panel of Fig. 6 and also presented in Fig. 8, where we compare the results for $\sigma = 40$ and $\sigma = 10$. For both magnetizations, the high-energy component is dominant ($f_{HE} \gtrsim 90$ per cent) in the limit of weak cooling, and drops with increasing cooling level. In the simulations with the lowest $\tau_{cool} = 0.06$, $f_{HE} \sim 25$ per cent for $\sigma = 10$, and $f_{HE} \sim 40$ per cent for $\sigma = 40$. Fig. 8 also demonstrates that f_{HE} is controlled by $\tau_{cool} \propto \gamma_{cr}^2/L_x$ rather than separately by γ_{cr} and L_x.

[6]The fact that the bulk spectrum peaks at lower energies in the smallest uncooled box ($L_x/(c/\omega_p) = 840$ in Fig. 7a) is due to the stochastic formation of a nearly stationary 'monster' plasmoid. In the simulations with cooling, the slow monsters also produce local maxima at low $\Gamma - 1 \lesssim 0.1$ (Fig. 6).

Downloaded from https://academic.oup.com/mnras/article/507/4/5625/6366935 by Columbia University user on 11 August 2022

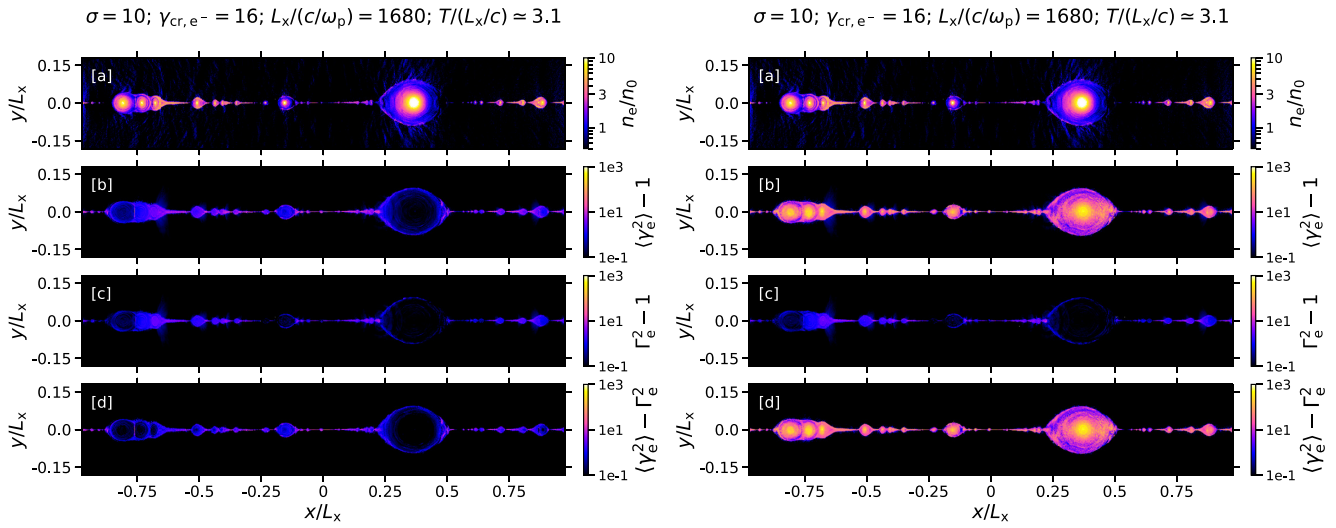

Figure 9. 2D snapshot of the reconnection layer at time $T \simeq 3.1\ L_x/c \simeq 10621\ \omega_p^{-1}$ for electrons (left-hand panel) and positrons (right-hand panel), in the hybrid simulation with magnetization $\sigma = 10$ and box size $L_x/(c/\omega_p) = 1680$. Only electrons are cooled, with a radiation energy density parametrized by $\gamma_{cr,e^-} = 16$. (a) Particle number density n, in units of the initialized (upstream) number density n_0; (b) Local average $\langle \gamma_e^2 \beta_e^2 \rangle = \langle \gamma_e^2 \rangle - 1$, which is proportional to the IC power per particle (the local average is calculated using the patches of 5 × 5 cells). (c) $\Gamma^2 - 1$, where Γ is the bulk Lorentz factor. (d) $\langle \gamma_e^2 \rangle - \Gamma^2$, which represents internal particle motions.

4.4 Hybrid experiment: cooled electrons and uncooled positrons

Magnetic reconnection in electron–ion plasmas gives the electrons the average energy $\sim \sigma_e m_e c^2$, where $\sigma_e = B_0^2/4\pi n_e c^2$ is the 'electron magnetization' (Rowan et al. 2017, 2019; Werner et al. 2018; Petropoulou et al. 2019). Bulk motions are primarily determined by the 'ion magnetization' $\sigma_i = (m_e/m_i)\sigma_e$ and become significantly slower when $\sigma_i < 1$. This case will be studied separately. Here, as a first step, we consider the simpler regime $\sigma_i > 1$.

As known from the simulations without cooling, the different particle masses become unimportant when $\sigma_i \gg 1$ and reconnection proceeds very similarly to that in pair plasma, with nearly equal energy spectra of ions and electrons. Cooling, however, breaks this symmetry, because only electrons can be efficiently cooled while ions retain the energy acquired from field dissipation. Then, a two-temperature plasma forms. A key question is whether there is energy transfer from the hot ions to the cool electrons. It could provide gradual electron heating inside plasmoids, keeping them at a much higher temperature than found for reconnection in pair plasmas. Then, thermal electron motions could dominate over the bulk plasmoid motions, and thus also dominate the IC power of the reconnection layer.

In general, the electron–ion energy exchange may occur via Coulomb collisions (at sufficiently high densities) or via collisionless plasma processes. We defer a complete analysis of this problem to a future work and here use our PIC simulations to study only the collisionless energy exchange (see also Zhdankin, Uzdensky & Kunz 2021, for a discussion of a similar problem in the context of plasma turbulence).

We devise a hybrid experiment mimicking a plasma composed of radiatively cooled electrons and hot ions. This experiment adopts the electron–positron composition, leveraging on the fact that reconnection in $\sigma_i \gg 1$ electron–ion plasmas is virtually indistinguishable from $\sigma \gg 1$ electron–positron reconnection (e.g. Guo et al. 2016), however we cool only one species (the electrons). This may be a useful first step for understanding collisionless energy exchange in electron–ion radiative reconnection.

Fig. 9 shows the structure of the reconnection layer in our hybrid experiment with $\sigma = 10$. Electrons are cooled with radiation density that corresponds to $\gamma_{cr,e^-} = 16$ (same as the fiducial value of γ_{cr} in SB20). We observe that the two species have identical bulk motions (panels c), and significantly different internal motions (panels d). Positrons, which are not cooled, are especially hot inside plasmoids – the average Lorentz factor of positrons is comparable to σ, which is typical for reconnection models without cooling. By contrast, electrons are cooled to a non-relativistic temperature, and their energy is dominated by the plasmoid bulk motion.

Fig. 10 shows the electron and positron spectra averaged over the reconnection region and time. The positron spectrum is similar to what was found in previous simulations with no cooling. It peaks at $\gamma_e - 1 \sim 4$ and has a high-energy tail extending beyond $\gamma_e \sim 10^2$. By contrast, the electron spectrum is similar to the simulations with full cooling (Section 4.3). Electrons have ultrarelativistic internal motions only in the thin regions of the main reconnection layer or in the secondary layers in between merging plasmoids, where particles are being actively heated/accelerated. In the hybrid experiment, these high-energy electrons carry a fraction $f_{HE} \sim 59$ per cent of the total IC power, remarkably similar to $f_{HE} \sim 52$ per cent found in a corresponding simulation where both species are cooled.

The main result of the hybrid simulation is that the behaviour of electrons is nearly the same as in the simulation with full cooling of both e^+ and e^-. This demonstrates that the energy transfer from the hot positrons to the cool electrons is inefficient, in the sense that it is unable to counteract the radiative losses of the electrons. This suggests that the electron component inside plasmoids will be kept cold also in electron–ion reconnection, at least when $\sigma_i \gg 1$. Then, Comptonization of radiation in the reconnection layer will remain dominated by the bulk motions of the plasmoid chain.

In the simulation that had strong cooling of both e^+ and e^- we observed the formation of density cavities inside plasmoids

Downloaded from https://academic.oup.com/mnras/article/507/4/5625/6366935 by Columbia University user on 11 August 2022

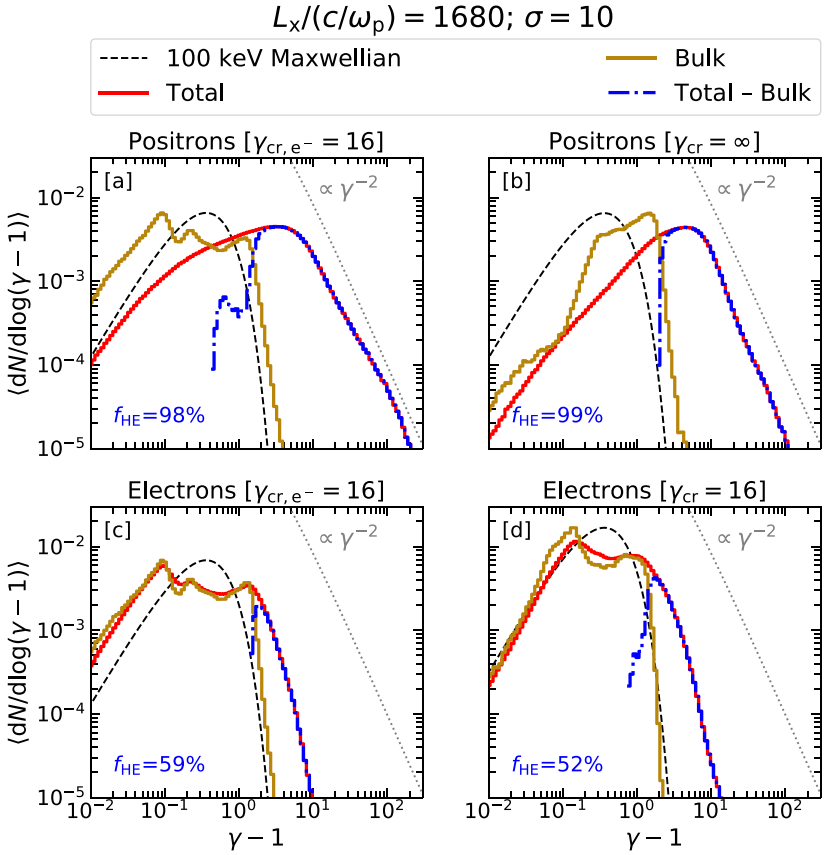

Figure 10. Particle energy spectra extracted from the reconnection region and averaged over time $2 \lesssim T/(L_x/c) \lesssim 5$ for three different simulations with magnetization $\sigma = 10$ and box size $L_x/(c/\omega_p) = 1680$. Two left-hand panels show the results of our hybrid experiment (same simulation as in Fig. 9): (a) positrons and (c) electrons. For comparison, two other simulations are shown on the right: (b) model with no cooling ($\gamma_{cr} = \infty$) and (d) model where both species are strongly cooled ($\gamma_{cr} = 16$). In these two models, both species are treated equally and the e^+/e^- spectra are identical. Each of the four panels shows the total energy spectrum (red; $\gamma = \gamma_e$), the bulk motion spectrum (golden-brown; $\gamma = \Gamma$), and their difference (dash-dotted blue). Each panel also shows a Maxwellian distribution with temperature of 100 keV (dashed black), normalized so that its peak matches the peak of the bulk energy spectrum. The dotted grey lines indicate the -2 slope that corresponds to equal IC power per decade in Lorentz factor.

(Section 4.1). These cavities practically disappear in the hybrid simulation. This is because, the inertia of the quasi-neutral plasma inside plasmoids is now much higher (the effective mass per particle is $\sim\sigma m_e$ because of the hot positrons) and therefore, the drag effect on the plasma distribution inside plasmoids is weaker.

5 MONTE CARLO RADIATIVE TRANSFER CALCULATIONS

We perform Monte Carlo simulations of X-ray emission expected from the reconnection layer using the radiative transfer code `Comp-Pair` (Beloborodov 2020). In the simulation, seed soft radiation is injected in the mid-plane of the reconnection layer, with a Planck spectrum of temperature $kT_s = 10^{-3} m_e c^2$, and the code follows the scattering of photons in the reconnection region, leading to formation of a Comptonized, hard X-ray spectrum. The radiative transfer is calculated in the region of $|x| < H = L_x/3$, where most of the scattering is expected to occur in a self-consistently produced $e^\pm$ plasma (Beloborodov 2017).

We use here a simplified setup of the transfer simulation which does not calculate $e^\pm$ production self-consistently. The inflow density n_0 is fixed in our PIC simulations, with no pair annihilation or injection of new $e^\pm$ pairs. We use seven snapshots of the PIC simulations spaced with time intervals of $0.5L_x/c$ between $T/(L_x/c) = 2$ and $T/(L_x/c) = 5$. The region $|x| < L_x$, $|y| < H$ is divided into 60×20 patches, and for each scattering event, the particle momentum is drawn from the local distribution function in the patch. The transfer simulation is then evolved in time with updating the distribution function every $0.5L_x/c$. The result of the radiative transfer depends on the overall normalization of the plasma density, which we parametrize using Thomson optical depth $\tau_T = H\sigma_T n_0$, defined in terms of the inflow density n_0. The optical depth is expected to be $\tau_T \sim 1$, depending on the compactness of the magnetic flare. Therefore, the photons sample the particle population on the photon mean free path to scattering, which is not smaller than H. We adjust τ_T to achieve the Compton amplification factor[7] $A \approx 10$, which is typically required for reproducing observed hard state spectra of accreting black holes, with a photon index of $\Gamma \sim 1.5$ (Beloborodov 2017). The corresponding optical depth is $\tau_T = 1.5$ for $\sigma = 10$, and $\tau_T = 0.5$ for $\sigma = 40$.

Fig. 11 shows the spectrum of radiation escaping from the reconnection region for the two models, with $\sigma = 10$ and $\sigma =$

[7]The factor A is the ratio of the average energy of escaping photons to the average energy of injected soft photons.

Downloaded from https://academic.oup.com/mnras/article/507/4/5625/6366935 by Columbia University user on 11 August 2022

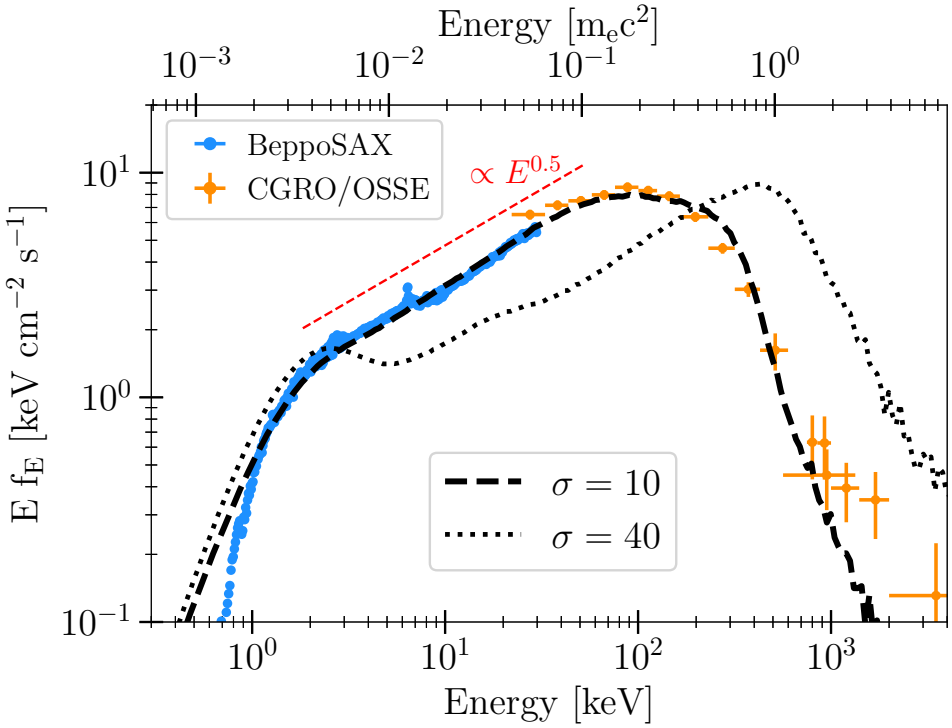

Figure 11. X-ray/γ-ray spectrum of Cygnus X-1 during its hard state, $Ef_E = E^2N(E)$. The 0.7–25 keV data (blue) are from *BeppoSAX* (Di Salvo et al. 2001; Frontera et al. 2001), and the 25–3500 keV data (orange) are from *CGRO/OSSE* (McConnell et al. 2002). The black dashed and dotted curves show the spectra formed by Comptonization in the reconnection layer in the models with $\sigma = 10$ (dashed) and $\sigma = 40$ (dotted), with the same strength of radiative cooling losses ($\gamma_{cr} = 16$) and Compton amplification factor ($A = 10$). The dashed red line indicates the power-law $N(E) \propto E^{-1.5}$. All the data are normalized with respect to *OSSE*.

40, adopting the same $\gamma_{cr} = 16$. The emitted spectrum varies with time as the reconnection proceeds, and Fig. 11 shows the emission averaged over the time interval $2 \lesssim T/(L_x/c) \lesssim 5$. We observe that the spectrum peaks around 100 keV and has a steeply decaying tail at higher energies. The model with $\sigma = 10$ is remarkably close to the typical hard-state of Cygnus X-1 observed in a broad-band of 1 − 1000 keV. For comparison, we overplot in Fig. 11 the data available from *BeppoSAX* and *CGRO/OSSE*. The deviation of the data from the model at low photon energies ($\lesssim 1$ keV) is expected from interstellar absorption. The excess at higher energies ($\gtrsim$1 MeV) may be interpreted as a contribution from coronal regions with $\sigma > 10$. Our simulations demonstrate that with increasing σ the Comptonized spectrum develops a stronger high-energy tail (compare the models with $\sigma = 10$ and $\sigma = 40$ in Fig. 11). The increased σ also shifts the spectral peak to above 100 keV. This shift is caused by the combination of two effects: the increased dispersion of the plasmoid speeds at high σ (Fig. 4), and the fact that high-energy particles contribute a larger fraction of IC power at higher magnetizations (Fig. 8).

6 SUMMARY

In this paper, we have performed 2D PIC simulations of relativistic magnetic reconnection with strong IC cooling, for conditions appropriate to the strongly magnetized regions of black hole coronae. Our main goal was to explore whether Comptonization by the Compton-cooled plasmoid chain in the reconnection layer can explain the observed hard X-ray spectra of accreting black holes, as proposed by Beloborodov (2017). Our work extends the investigation of SB20 to higher magnetizations up to $\sigma = 40$ and includes the Monte Carlo radiative transfer simulations of Comptonization in the reconnection region using the particle momentum distribution directly derived from the PIC simulations. Our main results are as follows.

(i) For a given magnetization σ, the energetics of the plasma in the reconnection layer is uniquely determined by the parameter $\tau_{cool} = t_{cool}/t_{adv}$, where t_{cool} is the time-scale for particles to cool to a non-relativistic energy (due to IC scattering), and $t_{adv} \approx L_x/c$ is the advection time-scale along the layer of size L_x. In the relevant limit of $\tau_{cool} \ll 1$, the majority of particles found inside the plasmoids are cooled to a non-relativistic internal energy per particle $\sim 0.5\tau_{cool} m_e c^2$ (if it still exceeds the Compton temperature of the radiation field, $kT_C \ll m_e c^2$). This makes thermal Comptonization unable to generate 100 keV X-rays.

(ii) In the strongly cooled regime, the IC power output is dominated by the bulk motions of a cold-chain of plasmoids, which are pulled against Compton drag by the magnetic stresses in the reconnection layer. The mean bulk 4-velocity along the layer is nearly independent of the cooling strength τ_{cool}^{-1} or the magnetization $\sigma \gg 1$, while the dispersion of bulk motions around the mean value tends to increase with increasing magnetization and τ_{cool} (i.e. for weaker cooling).

(iii) Particles accelerated in the reconnection layer on a time-scale faster than the IC losses form a high-energy tail in the particle spectrum. They are localized in thin regions of the main layer or of secondary layers between merging plasmoids. In the limit of strong cooling, we find that the fraction of radiated IC power contributed by the high-energy tail is ∼25 per cent for $\sigma = 10$ and ∼40 per cent for $\sigma = 40$.

Downloaded from https://academic.oup.com/mnras/article/507/4/5625/6366935 by Columbia University user on 11 August 2022

(iv) Comptonization of seed soft photons in the reconnection layer with $\sigma = 10$ closely reproduces the typical X-ray spectrum observed in the hard state of accreting black holes (e.g. with a power-law index of photon flux density $\lesssim 1.8$). It has a peak near 100 keV, which is shaped by the bulk motions of cold plasmoids. At higher σ the peak shifts to higher energies and the MeV tail of the spectrum increases.

Our simulations adopt an electron–positron plasma, and we defer a study of radiative reconnection in electron–ion plasmas to Part II of this series. However, in this work, we have also presented a strategy for mimicking a plasma composed of radiatively cooled electrons and hot ions, by performing a hybrid experiment in which we still adopt an electron–positron composition, but cool only one species (the electrons). Then, the positrons play the role of ions (which do not suffer radiative losses) with a reduced mass $m_i = m_e$. This experiment is likely to bear similarities to the full electron–ion model with $m_i \gg m_e$, in view of the known similarity of electron–positron and electron–ion relativistic reconnection in the regime of $\sigma \gg 1$ and negligible cooling.

Our hybrid experiment shows that the two species do not equilibrate, i.e. energy transfer from the uncooled positrons to the cooled electrons is not sufficiently fast to offset the IC losses of the electrons. As a result, the electron energies remain dominated by the bulk motions in the plasmoid chain. Thus, the cold-chain Comptonization model may also apply to radiative relativistic reconnection in electron–ion plasmas.

Our simulations are 2D, and we refer to SB20 for a demonstration of the fact that radiative 3D simulations lead to the same conclusions as their 2D counterparts. We refer to Part II of this series for an investigation of radiative reconnection in electron–ion plasmas, in the transrelativistic regime $\sigma \sim 1$. In the future, it may also be useful to investigate how the results change in the presence of a strong guide field, comparable to the reconnecting fields.

ACKNOWLEDGEMENTS

This paper benefited from useful discussions with Riley M. T. Connors, Javier A. García, Victoria Grinberg, Guglielmo Mastroserio, and James F. Steiner. We thank Andrzej Zdziarski for sharing details pertaining to the hard state observations of Cygnus X-1. NS acknowledges the support from Columbia University Dean's fellowship. LS acknowledges support from the Sloan Fellowship, the Cottrell Scholars Award, NASA 80NSSC20K1556, National Science Foundation (NSF) PHY-1903412, and Department of Energy (DoE) DE-SC0021254. AMB is supported by National Science Foundation grants AST-1816484 and AST-2009453, Simons Foundation grant #446228, and the Humboldt Foundation. This project made use of the following computational resources: Habanero and Terremoto HPC clusters at Columbia University, and Cori of National Energy Research Scientific Computing Center (NERSC).

DATA AVAILABILITY

The data underlying this article will be shared on reasonable request to the authors.

REFERENCES

Ball D., Sironi L., Özel F., 2018, ApJ, 862, 80
Beloborodov A. M., 1999, ApJ, 510, L123
Beloborodov A. M., 2017, ApJ, 850, 141
Beloborodov A. M., 2020, preprint (arXiv:2011.07310)
Bhattacharjee A., Huang Y.-M., Yang H., Rogers B., 2009, Phys. Plasmas, 16, 112102
Birdsall C. K., Langdon A. B., 1991, Plasma Physics via Computer Simulation
Buneman O., 1993, in 'Computer Space Plasma Physics', Terra Scientific, Tokyo, p. 67
Chashkina A., Bromberg O., Levinson A., 2021, MNRAS, preprint (arXiv:2106.15738)
Di Salvo T., Done C., Życki P. T., Burderi L., Robba N. R., 2001, ApJ, 547, 1024
Fender R. P., Belloni T. M., Gallo E., 2004, MNRAS, 355, 1105
Fender R. P., Homan J., Belloni T. M., 2009, MNRAS, 396, 1370
Frontera F. et al., 2001, ApJ, 546, 1027
Galeev A. A., Rosner R., Vaiana G. S., 1979, ApJ, 229, 318
Guo F. et al., 2016, ApJ, 818, L9
Guo F., Li H., Daughton W., Liu Y.-H., 2014, Phys. Rev. Lett., 113, 155005
Guo F., Li X., Daughton W., Kilian P., Li H., Liu Y.-H., Yan W., Ma D., 2019, ApJ, 879, L23
Hakobyan H., Petropoulou M., Spitkovsky A., Sironi L., 2021, ApJ, 912, 48
Harris E. G., 1962, Il Nuovo Cimento, 23, 115
Hoshino M., Lyubarsky Y., 2012, Space Sci. Rev., 173, 521
Huang Y.-M., Bhattacharjee A., 2012, Phys. Rev. Lett., 109, 265002
Kagan D., Milosavljević M., Spitkovsky A., 2013, ApJ, 774, 41
Kagan D., Sironi L., Cerutti B., Giannios D., 2015, Space Sci. Rev., 191, 545
Krawczynski H., 2021, ApJ, 906, 34
Liu B. F., Mineshige S., Shibata K., 2002, ApJ, 572, L173
Loureiro N. F., Schekochihin A. A., Cowley S. C., 2007, Phys. Plasmas, 14, 100703
Loureiro N. F., Samtaney R., Schekochihin A. A., Uzdensky D. A., 2012, Phys. Plasmas, 19, 042303
Lyubarsky Y., Liverts M., 2008, ApJ, 682, 1436
Lyubarsky Y. E., 2005, MNRAS, 358, 113
McClintock J. E., Remillard R. A., 2006, Black Hole Binaries, 39, 157
McConnell M. L. et al., 2002, ApJ, 572, 984
Mehlhaff J. M., Werner G. R., Uzdensky D. A., Begelman M. C., 2020, MNRAS, 498, 799
Mirabel I. F., Rodríguez L. F., 1999, ARA&A, 37, 409
Nalewajko K., Uzdensky D. A., Cerutti B., Werner G. R., Begelman M. C., 2015, ApJ, 815, 101
Nalewajko K., Yuan Y., Chruślińska M., 2018, J. Plasma Phys., 84, 755840301
Parfrey K., Giannios D., Beloborodov A. M., 2015, MNRAS, 446, L61
Petropoulou M., Sironi L., 2018, MNRAS, 481, 5687
Petropoulou M., Sironi L., Spitkovsky A., Giannios D., 2019, ApJ, 880, 37
Ripperda B., Bacchini F., Philippov A. A., 2020, ApJ, 900, 100
Rowan M. E., Sironi L., Narayan R., 2017, ApJ, 850, 29
Rowan M. E., Sironi L., Narayan R., 2019, ApJ, 873, 2
Sironi L., Beloborodov A. M., 2020, ApJ, 899, 52
Sironi L., Spitkovsky A., 2014, ApJ, 783, L21
Sironi L., Petropoulou M., Giannios D., 2015, MNRAS, 450, 183
Sironi L., Giannios D., Petropoulou M., 2016, MNRAS, 462, 48
Spitkovsky A., 2005, in Bulik T., Rudak B., Madejski G., eds, AIP Conf. Proc. Vol. 801, Astrophysical Sources of High Energy Particles and Radiation. Am. Inst. Phys., New York, p. 345
Sridhar N., García J. A., Steiner J. F., Connors R. M. T., Grinberg V., Harrison F. A., 2020, ApJ, 890, 53
Tajima T., Shibata K., 1997, Plasma Astrophysics
Tamburini M., Pegoraro F., Di Piazza A., Keitel C. H., Macchi A., 2010, New J. Phys., 12, 123005
Uzdensky D. A., Loureiro N. F., Schekochihin A. A., 2010, Phys. Rev. Lett., 105, 235002
van der Klis M., 1989, ARA&A, 27, 517
Vay J.-L., 2008, Phys. Plasmas, 15, 056701
Werner G. R., Uzdensky D. A., 2017, ApJ, 843, L27
Werner G. R., Uzdensky D. A., Cerutti B., Nalewajko K., Begelman M. C., 2016, ApJ, 816, L8
Werner G. R., Uzdensky D. A., Begelman M. C., Cerutti B., Nalewajko K., 2018, MNRAS, 473, 4840
Werner G. R., Philippov A. A., Uzdensky D. A., 2019, MNRAS, 482, L60
Yuan Y., Spitkovsky A., Blandford R. D., Wilkins D. R., 2019, MNRAS, 487, 4114
Zdziarski A. A., Gierliński M., 2004, Progr. Theoret. Phys. Suppl., 155, 99
Zenitani S., Hoshino M., 2001, ApJ, 562, L63

Downloaded from https://academic.oup.com/mnras/article/507/4/5625/6366935 by Columbia University user on 11 August 2022

Zhang H., Sironi L., Giannios D., 2021, preprint (arXiv:2105.00009)
Zhdankin V., Uzdensky D. A., Kunz M. W., 2021, ApJ, 908, 71

APPENDIX A: SIMULATION PARAMETERS

We present in Table A1 the input parameters of our simulations (left-hand side) and the main outcomes (right-hand side).

APPENDIX B: PLASMOID PROPERTIES

We identify plasmoids based on the z-component of the magnetic vector potential (A_z), as described in Sironi et al. (2016). We first identify O-points as maxima of A_z, which correspond to the plasmoid centres. Along the reconnection layer, the two local minima around

Table A1. List of numerical input parameters corresponding to different simulations, and the resulting plasma properties.

σ[1]	γ_{cr}[2]	Domain size[3]		τ_{cool}[4]	$\langle\mathcal{E}_{int}\rangle$[5]	$\langle\Gamma\rangle-1$[6]	$\langle u_x(x>0)\rangle_x$[7]	$\langle\sigma_{u_x}\rangle_x$[8]	f_{HE}[9] (per cent)
		$L_x/(c/\omega_p)^a$	$L_x/(r_{0,\,hot})^b$						
				Very strongly magnetized regime					
40	16	840	132.8	0.48	0.46	0.38	0.98	0.76	77
40	22.6	840	132.8	0.96	0.75	0.30	0.80	0.77	89
40	32	840	132.8	1.92	1.18	0.38	0.72	0.76	92
40	45	840	132.8	3.85	1.71	0.36	0.78	0.68	96
40	∞	840	132.8	∞	7.52	0.26	0.56	0.76	100
40	16	1680	265.6	0.24	0.19	0.40	1.04	0.72	59
40	22.6	1680	265.6	0.48	0.39	0.39	0.94	0.82	78
40	32	1680	265.6	0.96	0.64	0.39	0.86	0.82	88
40	45	1680	265.6	1.92	1.21	0.41	0.88	0.82	93
40	∞	1680	265.6	∞	7.20	0.44	1.08	0.96	100
40	16	3360	531.2	0.12	0.13	0.35	0.92	0.60	51
40	22.6	3360	531.2	0.24	0.20	0.36	1.04	0.80	64
40	32	3360	531.2	0.48	0.39	0.42	1.10	0.82	77
40	45	3360	531.2	0.96	0.76	0.36	0.92	0.82	89
40	∞	3360	531.2	∞	8.29	0.41	0.93	0.86	100
40	16	6720	1062.4	0.06	0.06	0.43	0.99	0.69	39
				Strongly magnetized regime					
10	11.3	420	132.8	0.96	0.35	0.36	0.48	0.25	71
10	8	840	265.6	0.24	0.09	0.17	0.58	0.34	44
10	11.3	840	265.6	0.48	0.19	0.32	0.80	0.44	58
10	16	840	265.6	0.96	0.32	0.43	1.02	0.56	71
10	22.6	840	265.6	1.92	0.53	0.46	1.04	0.58	84
10	32	840	265.6	3.84	0.82	0.51	1.28	0.62	89
10	8	1680	531.2	0.12	0.03	0.13	0.58	0.30	34
10	11.3	1680	531.2	0.24	0.08	0.22	0.82	0.48	46
10	16	1680	531.2	0.48	0.15	0.27	0.84	0.52	52
10	16†	1680	531.2	0.48	0.09	0.20	0.72	0.50	59
10	22.6	1680	531.2	0.96	0.39	0.40	1.02	0.58	77
10	32	1680	531.2	1.92	0.64	0.50	1.20	0.62	87
10	8	3360	1062.4	0.06	0.01	0.08	0.52	0.20	23
10	11.3	3360	1062.4	0.12	0.03	0.16	0.68	0.30	28
10	16	3360	1062.4	0.24	0.07	0.37	1.06	0.48	39
10	11.3	6720	2124.8	0.06	0.02	0.12	0.68	0.26	25
10	16	6720	2124.8	0.12	0.03	0.24	0.90	0.36	30

Note. The first five columns contain numerical and physical input parameters, and the last five columns contain the plasma parameters obtained from the simulations. All simulations are performed for a duration of $T \sim 5L_x/c$. The description of each column is as follows. [1]Magnetization in the upstream plasma; [2]Critical Lorentz factor – a proxy for the intensity of incident photon field ($\gamma_{cr} = \infty$ implies no IC cooling, and smaller γ_{cr} implies greater IC cooling; see equation (4)); [3]Half-length of the computational domain along the x-direction in units of ^{a}plasma skin depth, and ^{b}post-reconnection Larmor radius $r_{0,hot} = \sqrt{\sigma}c/\omega_p$, respectively; [4] τ_{cool}, as defined in equation (13); [5, 6]mean internal and bulk energy per particle in units of rest mass energy ($m_e c^2 = 511$ keV); [7]bulk outflow dimensionless 4-velocity along the reconnection layer averaged over one half of the box; [8]spread of the 4-velocity distribution averaged over one half of the box; [9]fractional IC power contributed by high-energy particles. The symbol † indicates the hybrid experiment (see Section 4.4) where only electrons are subjected to IC cooling while positrons are not, i.e. $\gamma_{cr,e^-} = 16$ and $\gamma_{cr,e^+} = \infty$.

Downloaded from https://academic.oup.com/mnras/article/507/4/5625/6366935 by Columbia University user on 11 August 2022

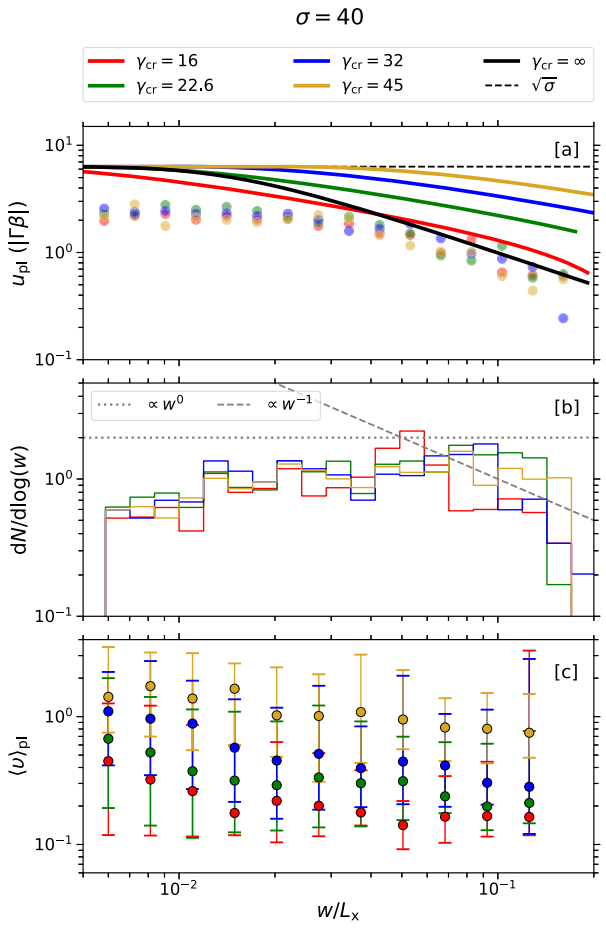

Figure B1. Plasmoid properties in a strongly magnetized ($\sigma = 40$) plasma, as a function of their width w/L_x and of the cooling strength γ_{cr} (red: $\gamma_{cr} = 16$, green: $\gamma_{cr} = 22.6$, blue: $\gamma_{cr} = 32$, golden brown: $\gamma_{cr} = 45$). The simulations are performed with a $L_x/(c/\omega_p) = 3360$ box, and each of the quantities displayed is averaged over $2 \lesssim T/(L_x/c) \lesssim 5$. Top panel (a): Each circular marker denotes the 90th percentile of plasmoid dimensionless 4-velocities for plasmoids of a given size. The solid black and coloured lines indicate the upper limit in the absence (equation B1) and presence (equation B2) of IC cooling, respectively. For comparison, the Alfvén limit is shown by the dashed horizontal line. Middle panel (b): Cumulative distribution of plasmoid widths $F(w) = dN/d\log w$. The expectations $F(w) \propto w^0$ (Huang & Bhattacharjee 2012) and $F(w) \propto w^{-1}$(Uzdensky et al. 2010; Loureiro et al. 2012) are depicted by the grey dotted and dashed lines, respectively. Bottom panel (c): Internal energy per particle (in units of $m_e c^2 = 511$ keV), averaged over all the particles inside a plasmoid. The filled circles denote the median values for a given plasmoid width, and the error bars denote the 10th and 90th percentiles.

each O-point correspond to two X-points. The largest of the two values of A_z at these two X-points identifies the equipotential line that we use as the plasmoid contour.

We define the plasmoid width w in the direction transverse to the main layer, and the plasmoid bulk velocity as the velocity of its O-point (plasmoids move nearly as rigid bodies). In Fig. B1, we describe the properties of plasmoids as a function of their width w, for different levels of IC cooling. Panel (a) quantifies the plasmoid maximum bulk 4-velocity (more precisely, circles indicate the values of the 90th percentile in each size bin). In the absence of IC cooling, the plasmoid 4-velocity when exiting the layer[8] is

$$\Gamma\beta \simeq \sqrt{\sigma}\tanh\left(\frac{\eta_{rec}}{\sqrt{\sigma}}\frac{L_x}{w}\right) \tag{B1}$$

which is indicated by the black line in panel (a). When strong Compton drag is included, the plasmoid bulk motion is regulated by the competition between bulk acceleration by magnetic field tension and Compton drag. As shown by SB20, this leads to a maximum 4-velocity

$$\Gamma\beta \simeq \sqrt{\sigma}\tanh\left(\frac{2n_0}{n'_{pl}}\frac{c/\omega_p}{w}\frac{\gamma_{cr}^2\beta}{\Gamma}\right), \tag{B2}$$

where n'_{pl}/n_0 is the plasmoid compression factor, defined as the ratio of the mean rest-frame density in the plasmoid to the upstream density. The curves corresponding to different levels of cooling are shown in panel (a) by the different colours (see legend). At each value of w, the maximum 4-velocity of a plasmoid will be controlled by the smallest between equation (B1) and equation (B2). The data points shown in panel (a) demonstrate that Compton drag does not appreciably slow down the plasmoids in our simulations. Also, regardless of the cooling level, smaller plasmoids are faster than larger plasmoids, yet they barely reach the Alfénic limit $\Gamma\beta \sim \sqrt{\sigma} \simeq 6.3$ predicted by Lyubarsky (2005) (indicated by the horizontal dashed line).

In the middle panel (b) of Fig. B1, we present the cumulative plasmoid size distribution $F(w) = dN/d\log(w)$. Regardless of the level of cooling, this can be modelled as a broken power law, with $F(w) \propto w^0$ (Huang & Bhattacharjee 2012) for small sizes and $F(w) \propto w^{-1}$ (Uzdensky et al. 2010; Loureiro et al. 2012) for larger plasmoids, $w/L_x \gtrsim 0.07$.

The bottom panel (c) of Fig. B1 shows the mean internal energy per particle inside plasmoids of different sizes. We generally find that larger plasmoids, which live longer, have time to cool down to lower temperatures. This effect is less pronounced for moderate cooling (yellow points for $\gamma_{cr} = 45$; here, all plasmoids stay rather hot), and more evident for stronger cooling. As expected, for plasmoids of a given size, the average internal energy per particle decreases for stronger cooling.

APPENDIX C: COMPUTATION OF THE INTERNAL ENERGY PER PARTICLE

The probability distribution function of a plasma described by a Maxwell–Jüttner distribution is

$$f_{MJ}(\gamma_e, \theta_e) = \frac{\gamma_e\sqrt{\gamma_e^2 - 1}\exp(-\gamma_e/\theta_e)}{\theta_e K_2\left(\frac{1}{\theta_e}\right)}, \tag{C1}$$

where $\theta_e = kT_e/m_e c^2$ is the dimensionless temperature parameter and K_2 is the modified Bessel function of the second kind. The internal energy per particle (in units of $m_e c^2$) can be written as

$$\mathcal{E}_{int} = \frac{\int_1^\infty \gamma_e f_{MJ}(\gamma_e, \theta_e)d\gamma_e}{\int_1^\infty f_{MJ}(\gamma_e, \theta_e)d\gamma_e} - 1. \tag{C2}$$

For values of θ_e in the range $[10^{-3}, 10^3]$, equation (C2) is solved for $\mathcal{E}_{int}(\theta_e)$. This can be used to find a mapping between the adiabatic index $\hat{\gamma}_e(\mathcal{E}_{int})$ and $\mathcal{E}_{int}$ using the relation $\theta_e = [\hat{\gamma}_e(\mathcal{E}_{int}) - 1]\mathcal{E}_{int}$. We

[8]For plasmoids that do not end their life by merging into a bigger plasmoid, this corresponds to the time when they are largest and fastest.

Downloaded from https://academic.oup.com/mnras/article/507/4/5625/6366935 by Columbia University user on 11 August 2022

then model this mapping by assuming that the adiabatic index is of the form

$$\hat{\gamma}_{\rm e} \equiv \frac{A + B\mathcal{E}_{\rm int}}{C + D\mathcal{E}_{\rm int}}, \tag{C3}$$

where the best-fitting values of the numerical coefficients are found to be $A \simeq 1.187$, $B \simeq 1.251$, $C \simeq 0.714$, and $D \simeq 0.936$. Note that the numerical coefficients satisfy $A/C \simeq 5/3$ and $B/D \simeq 4/3$ in the non-relativistic ($\mathcal{E}_{\rm int} \to 0$) and ultrarelativistic ($\mathcal{E}_{\rm int} \to \infty$) limits, respectively.

In order to estimate the internal energy per particle ($\mathcal{E}_{\rm int}$) and the temperature ($\theta_{\rm e}$) in the fluid frame, we assume a perfect and isotropic fluid for which the stress-energy tensor is given by

$$T^{\mu\nu} = (e + p)U^{\mu}U^{\nu} - pg^{\mu\nu}, \tag{C4}$$

where p is the pressure, U^{μ} is the fluid dimensionless four-velocity, $g^{\mu\nu}$ is the flat-space Minkowski metric, and $e = n'_{\rm e}m_{\rm e}c^2 + u_{\rm e}$ is the rest-frame energy density of electrons, where $n'_{\rm e}$ is the particle number density in the fluid frame, and $u_{\rm e} = p_{\rm e}/(\hat{\gamma} - 1)$ is the internal energy density (like electron pressure $p_{\rm e}$, it is also defined in the fluid frame). The dimensionless internal energy per particle in the fluid frame is $\mathcal{E}_{\rm int} = u_e/n'_e m_e c^2$. Using the transformation of $T^{\mu\nu}$ one can express $\mathcal{E}_{\rm int}$ in terms of the lab-frame quantities,

$$\mathcal{E}_{\rm int} = \frac{[T_{\rm e}^{00}/n_{\rm e}m_{\rm e}c^2 - \Gamma]\Gamma}{1 + \hat{\gamma}_{\rm e}(\Gamma^2 - 1)} = \frac{[\bar{\gamma}_{\rm e} - \Gamma]\Gamma}{1 + \hat{\gamma}_{\rm e}(\Gamma^2 - 1)}, \tag{C5}$$

where Γ is the fluid Lorentz factor, $\bar{\gamma}_{\rm e}$ is the average particle Lorentz factor, $T_{\rm e}^{00} = \bar{\gamma}_{\rm e}n_{\rm e}m_{\rm e}c^2$ is the energy density, and $n_{\rm e} = \Gamma n'_{\rm e}$ is the number density, all measured in the lab frame.

APPENDIX D: ASSESSMENT OF QUASI-STEADY STATE

Many of the results presented in this paper are obtained by averaging in the interval $2 \lesssim T/(L_{\rm x}/c) \lesssim 5$. As we describe in Section 2, at even earlier times ($T/(L_{\rm x}/c) \lesssim 2$), the reconnection layer is not in steady state – this is the time needed for the two reconnection fronts to advect out of the box the hot plasma initialized in the current sheet.

In Fig. D1, we subdivide the range $2 \lesssim T/(L_{\rm x}/c) \lesssim 5$ in intervals of duration $L_{\rm x}/c$, and in each interval we compute the time-averaged total [left] and bulk [right] spectrum. We employ our reference simulation with $\sigma = 40$, $\gamma_{\rm cr} = 16$, and $L_{\rm x}/(c/\omega_{\rm p}) = 3360$, whose spectrum is shown in Fig. 6(c). The figure convincingly demonstrates that the layer has achieved a quasi-steady state.

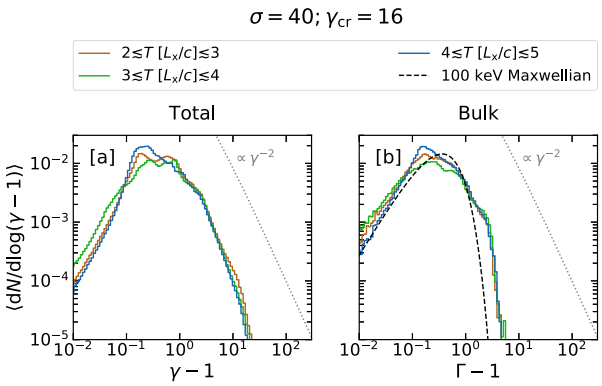

Figure D1. Total (panel a) and bulk (panel b) energy spectra, time-averaged in the intervals $2 \lesssim T/(L_{\rm x}/c) \lesssim 3$ (golden-brown), $3 \lesssim T/(L_{\rm x}/c) \lesssim 4$ (green), and $4 \lesssim T/(L_{\rm x}/c) \lesssim 5$ (blue). We employ our reference simulation with $\sigma = 40$, $\gamma_{\rm cr} = 16$, and $L_{\rm x}/(c/\omega_{\rm p}) = 3360$. Panel (b) also shows a representative 100 keV Maxwellian (dashed black curve). Both panels demonstrate that the system achieves a quasi-steady state for $T/(L_{\rm x}/c) \gtrsim 2$.

This paper has been typeset from a TEX/LATEX file prepared by the author.

Downloaded from https://academic.oup.com/mnras/article/507/4/5625/6366935 by Columbia University user on 11 August 2022